FABRICATION AND CHARACTERIZATION OF

METAL OXYCARBIDE THIN FILMS

by

Benjamin Willis Schmidt

Dissertation

Submitted to the Faculty of the

Graduate School of Vanderbilt University

in partial fulfillment of the requirements

for the degree of

DOCTOR OF PHILOSOPHY

in

CHEMICAL ENGINEERING

MAY, 2010

Nashville, Tennessee

Approved:

Professor Bridget R. Rogers

Professor Kenneth A. Debelak

Professor Timothy P. Hanusa

Professor G. Kane Jennings

Professor M. Douglas LeVan

To my bride-to-be, Katie, for taking this journey with me

and

To my parents, Roger and Sheila, for their continual love and support

ACKNOWLEDGEMENTS

I would like to thank my research advisor, Professor Bridget Rogers, for her support, guidance, and patience through the past few years.

I would also like to thank my committee, Professor Ken Debelak, Professor Tim Hanusa, Professor Kane Jennings, and Professor Doug LeVan. Professor Hanusa was instrumental in the development of our precursors, which drove this whole project.

I am also thankful to everyone who helped my work move along. To the students in Prof. Hanusa's lab, for developing and supplying the precursors. To Mark Holmes and Robin Midgett, for fixing almost anything and finding pretty much any tool I could ever need. To Mary Gilleran and the office staff, for making sure everything behind the scenes went smoothly.   To the equipment vendors, who were helpful no matter how trivial my questions were.

I am especially thankful to my friends and family for their love and support. To the members of the Rogers group – Dr. Zhe Song, Dr. Bob Geil, Dr. Mekha George, Dr. Nirav Vora, Jimi Burst, and Bobby Harl – for your assistance and camaraderie. To my best friend, Katie Bradshaw, for telling it like it is and constantly pushing me to succeed. To my family – Roger, Sheila, Jenna, and Michael – for always being there and encouraging me to expand my horizons.

LIST OF TABLES

LIST OF FIGURES

TABLE OF CONTENTS

CHAPTER I

BACKGROUND

Introduction

Ceramics comprise a wide class of materials characterized by a number of interesting properties including high thermal stability, high strength, and chemical inertness. Barsoum [1] defines ceramics as "solid compounds that are formed by the application of heat, and sometimes heat and pressure, comprising at least two elements provided one of them is a non-metal or a nonmetallic elemental solid. The other element(s) may be a metal(s) or another nonmetallic elemental solid(s)." The author further illustrates the expansiveness of the ceramics realm by nothing that "what is neither a metal, a semiconductor or a polymer is a ceramic." In this work, we will investigate low temperature (< 1000 °C) fabrication of two types of ceramic materials that are important for microelectronic or thermal protection applications.

Field effect transistor gate dielectrics

The International Technology Roadmap for Semiconductors (ITRS) is a set of goals established by the semiconductor industry related to challenges in the scaling of microelectronic devices. The 2007 edition of the ITRS [2] dictates that the thickness of the gate oxide in metal-oxide-semiconductor field-effect transistors (MOSFET) should be 1 nm or less. At such small thicknesses silicon dioxide gate oxides exhibit large leakage currents due to electron tunneling from the substrate to the gate metal. Leakage current

causes increased power consumption and difficulty maintaining the switching state of the MOSFET. Aluminum oxide is one of several materials under investigation to replace SiO_2 as the gate dielectric [3].

The basic structure of a MOSFET is shown in Figure 1.1. The gate material is separated from the substrate by a low-conductivity dielectric layer. The substrate is typically doped to dictate the number and type of charge carriers. The substrate is considered n-type if the majority of carriers are electrons or p-type if the majority of carriers are holes. The structure acts as a parallel plate capacitor when a voltage bias is placed on the gate relative to the substrate. Carriers in the substrate are either attracted to or repelled from the substrate/dielectric interface depending on the polarity of the gate bias. At a condition known as "inversion", the concentration of minority carriers (e.g., holes in an n-type substrate) at the interface exceeds the concentration of majority carriers, thus creating a conducting channel of charged carriers at the substrate/dielectric interface. Once the channel is established, current can flow between the source and drain electrodes if a bias is applied.
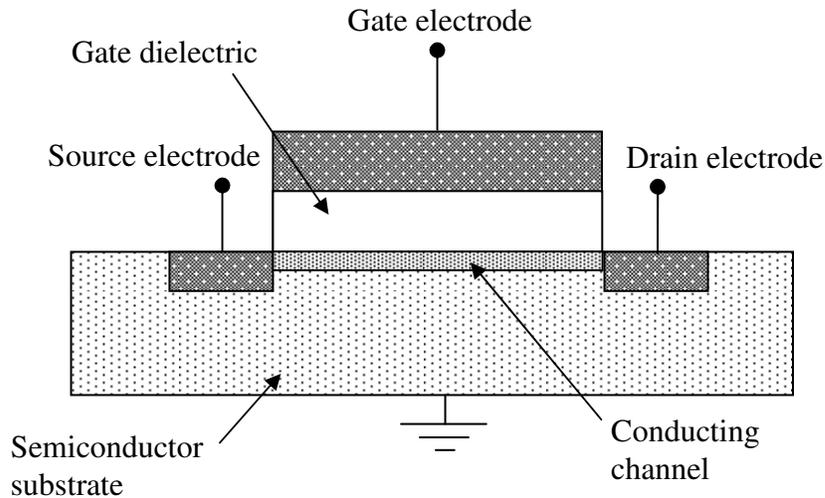
Figure 1.1 - Schematic of MOSFET device

The abandonment of silicon dioxide as the gate dielectric and arrival of a new material is the first fundamental change to the MOSFET in about 40 years. There is a need to maintain the capacitance in the device as if the thin SiO_2 was still there, but without the negative leakage effects due to tunneling. This may be accomplished with the use of materials with higher dielectric constants than SiO_2 ($\varepsilon_r = 3.9$). Aluminum oxide ($\varepsilon_r \sim 9$) possesses several qualities that make it a good candidate as the replacement material, such as large band offsets, thermal stability on silicon, and amorphous character [4].

High temperature materials

Many processes are enhanced by operation at high temperatures. For example, reaction and diffusion rates can be increased by increasing the system temperature in accordance with the Arrhenius equation. In production processes, this could result in higher throughput and increased profits. In another example, heat cycles such as those in

jet engines show increased thermal efficiencies as the temperature difference between the hot source and cold sink increases. Since the cold sink is often at ambient temperature, it makes sense to try to increase the temperature of the hot source. Higher efficiencies suggest that less fuel is required for a given application, which reduces fuel costs and total weight. As a final example, reaction selectivity or equilibrium may dictate that high temperatures are required to achieve a desired product. Metal carbide formation by carbothermal reduction of oxides require temperatures in excess of 1100 °C [5]. Thus, there are definite benefits for operating systems at increased temperatures. High temperature applications require appropriate materials that can not only withstand the temperature, but can also maintain useful chemical, electrical, or mechanical properties.

Ultrahigh temperature materials (UHTMs) are a class of compounds that are stable above 1600 °C. Several applications for UHTMs are hypersonic flight vehicles, reusable space orbiters, and propulsion systems [6]. Currently thermal protection systems are composed of carbon-carbon composites and silicon-based materials such as SiO_2 and SiC. Silica is formed in oxidizing atmospheres, and at temperatures above ~1600 °C the silica begins to soften and vaporize [7]. Novel high temperature materials are needed to improve upon the capabilities of the silica-based materials.

The carbides, borides, and nitrides of refractory metals are excellent candidates for extreme environments due to their very high melting temperatures. Table 1.1 lists the melting temperature of several refractory binary compounds. Hafnium carbide and tantalum carbide have the two highest melting temperatures of known binary compounds.

Table 1.1. Melting temperatures of binary refractory compounds [8]

Metal	Boride (MB$_x$)	Carbide (MC$_x$)	Nitride (MN$_x$)
Ti	2980	3067	2950
Zr	3040	3420	2980
Hf	3250	3928	3387
V	2100	2187-2830	2177
Nb	3050	3080-3600	~2400
Ta	3200	3330-3950	3093
Cr	2170	1810	-
Mo	2100	2520	-
W	2600	2870	-

Oxidation of the UHTMs is a major concern. In comparison with the parent compound, refractory oxides are generally more brittle, have lower melting temperatures, and exhibit inferior thermal shock resistance (due to a combination of reduced thermal conductivity and an increased coefficient of thermal expansion). The development of materials with good oxidation resistance at high temperatures has been a major driving force in UHTM research [6].

The borides of the Group IV elements (Ti, Zr, Hf) have shown the most promising oxidation resistance of the binary compounds [9]. The oxidation of HfB$_2$ in air is summarized in reference [10] and shown in Equation 1-1.

$$HfB_2(c) + \frac{5}{2}O_2(g) \rightarrow HfO_2(c) + B_2O_3(l) \tag{1-1}$$
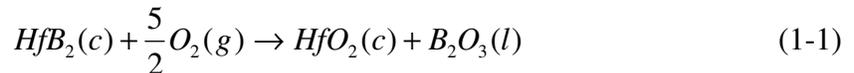
Oxidation begins around 700 °C. At temperatures up to approximately 1100 °C, HfO_2 and B_2O_3 form a continuous surface layer. The oxide thickness increases parabolically as a function of time such that the rate of change of oxide thickness decreases at longer times. This suggests that further oxidation is limited by the rate of oxygen transport through the liquid boria. At temperatures between 1100 and 1400 °C, boria begins to evaporate. At 1400 °C the boria is mostly gone. Without the boria as a diffusion barrier, oxygen diffuses quickly through the crystalline HfO_2 lattice to the virgin material and oxidizes the HfB_2 with linear kinetics. The parabolic oxidation regime has been extended by introducing additives such as SiC or Ta [10]. In the case of SiC additions, a borosilicate glassy layer is formed with higher viscosity and lower volatility than the pure boria.

The refractory carbides and nitrides are generally considered inferior to the diborides in terms of oxidation resistance [9]. However, several authors have reported that the oxide scale that is produced from oxidation of HfC consists of two layers: a porous outside scale, and a dense inner scale [11-13]. The outer scale was mainly oxide, while the inner scale contained approximately 25 at.% carbon [14] and was identified as an oxycarbide layer. The oxycarbide layer has been observed even after heat treatments at 2060 °C [15]. Bargeron [15] reported that the oxycarbide layer was a better oxygen diffusion barrier than either the porous oxide scale or the virgin carbide material. The composition of the oxycarbide layer is not well understood, and work is currently underway to try and reproduce it as a standalone diffusion barrier material.

<p style="text-align:center">Motivation</p>

Ceramic carbides and oxycarbides of aluminum and hafnium possess useful properties for electrical and thermal applications. However, as is the case with many ceramics, the inherent inertness that is so helpful also makes processing difficult.

Processing methods for bulk ceramics

Bulk ceramics are typically fabricated through powder processing techniques. Starting powders can be obtained through reactions at relatively high temperatures, as shown below for the production of HfC powders [5].

- Carbothermal reduction: $HfO_2 + C \rightarrow HfC$ + products (1900-2200 °C in H_2)

- Carburizaiton: Hf + hydrocarbons $\rightarrow$ HfC + products (2030-2130 °C)

- Vapor synthesis: $HfCl_4 + H_2$ + hydrocarbon $\rightarrow$ HfC + products (2100 °C)

The powders are then pressed into desired shapes. Temperatures and pressures in the pressing tools can reach 1000+ °C and 100+ GPa, respectively. The pressed shapes are then sintered at high temperatures to bond the particles and densify the ceramic.

There are several drawbacks to powder fabrication techniques. The quality of the final product depends on the quality of the starting powder. Inhomogeneous mixtures and particle size distributions can affect the sintering behavior and therefore affect the final properties. Also, sintering aids can add impurities to the material. Alternative processing methods are desired to achieve greater process control.

Processing methods for coatings

Coating processes are ideal for producing surface properties different from those of the bulk material. For example, it is possible to coat a lightweight structural material with a hard ceramic coating with minimal weight gain to the overall system. There are several vapor-phase and liquid-phase coating technologies available based on the specific application. In this work, chemical vapor deposition will be used for film deposition.

Our Approach

Chemical vapor deposition is an effective method for coating many types of engineered structures. The choice of precursor dictates many attributes of the process, such as the temperature of the reaction or decomposition, as well as impurities or by-products. There are several classes of vapor phase precursor structures, but in order to be useful, any precursor must exhibit certain basic properties:

- Adequate vapor pressure at mild temperatures to achieve necessary mass flow to the reaction zone

- Large temperature window between vaporization and decomposition

- Decomposition pathway that results in volatile by-products

Precursors can be engineered through novel chemistry pathways to improve their properties. For example, adding long alkyl chains can disrupt crystalline packing and therefore increase volatility. Also, substituting fluorine atoms in place of methyl group ligands reduces intermolecular interaction and raises volatility. On the other hand, by increasing chain lengths one risks the possibility that by-products are not volatile and instead become part of the film. Similarly with the addition of fluorine, there is a

possibility of the incorporation of undesired fluorine atoms into the film which may change the film properties. These are just a few examples of the considerations to make when developing new precursor materials.

Aluminum precursors

Two common aluminum-based precursors are trimethylaluminum (TMA) and aluminum tri-isopropoxide (ATI). TMA consists of three methyl groups attached to an aluminum atom. It is a liquid at room temperature with a vapor pressure of approximately 100 Torr at 60 °C [16]. It is a versatile precursor and has been used for the deposition of aluminum metal [17], oxides [18], nitrides [19], arsenides [20], and other materials. However, TMA is pyrophoric and therefore requires certain handling procedures. ATI on the other hand is air-stable. ATI is made up of three isopropyl ligands, each bonded to aluminum through an oxygen linkage. One advantage that ATI has over TMA is that ATI does not require a co-reactant gas for the deposition of aluminum oxide films [21, 22]. The use of a so-called "single source" precursor can reduce the complexities of handling multiple gas streams and their individual effects on the process. A drawback of ATI is that the metal-oxygen bonds bridge with nearby molecules to form heavy oligomers, thus reducing its vapor pressure [23].

A novel precursor solution is the use of dimethylaluminum isopropoxide (DMAI). DMAI is a heteroleptic (contains multiple ligand structures attached to metal atom) compound with similarities to TMA and ATI. The structure of DMAI consists of two methyl groups bonded to an aluminum atom and one isopropyl group bonded to aluminum through an oxygen atom. The compound is a liquid at room temperature and

exhibits a vapor pressure of approximately 5 Torr at ambient temperatures, as shown in
Figure 1.2. Several studies have shown that DMAI can be used to deposit oxide films
[24-28], but it would be interesting to investigate the oxycarbide films that could be
deposited based on the stoichiometry of the precursor.
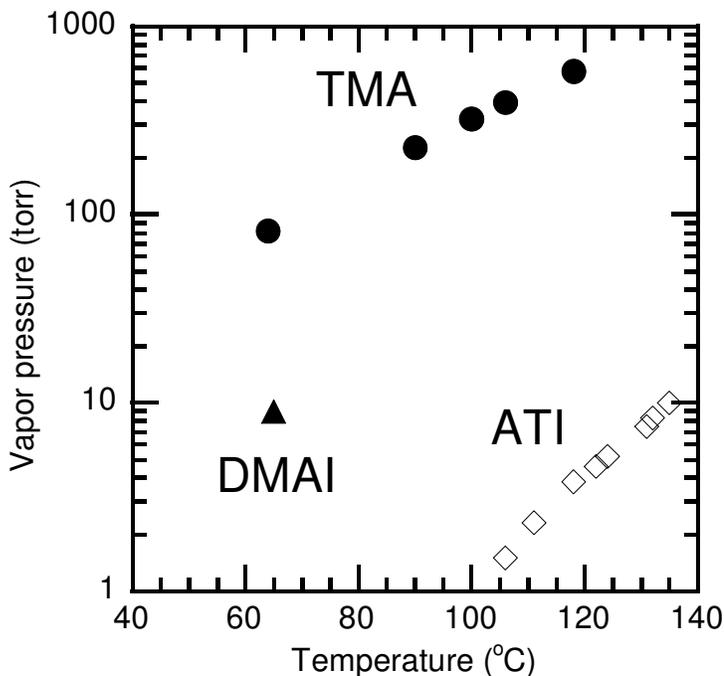
Figure 1.2 - Vapor pressures of trimethylaluminum (TMA), dimethylaluminum
isopropoxide (DMAI), and aluminum tri-isopropoxide (ATI)

Hafnium precursors

In a similar fashion as the aluminum studies, we are interested in developing a
single source precursor for hafnium carbide films. The precursor should contain only
hafnium, carbon, and hydrogen. The metallocene family of compounds was chosen due
to the thermal stability and possibilities for ligand tailoring.

10

Goals of this work

The goals of this project were to investigate fabrication strategies for the production of aluminum oxycarbide and hafnium oxycarbide films. The relationships between process conditions and film properties were identified through a variety of characterization techniques using x-ray, ion, photon, or electrical probes as described below.

X-ray photoelectron spectroscopy (XPS) is a surface-sensitive technique that provides elemental identification and chemical bonding information. Soft x-rays irradiate the sample under vacuum, and the kinetic energies of emitted photoelectrons are analyzed. Electron binding energies (BE) are calculated based on the kinetic energy (KE), incident x-ray energy (hν), and spectrometer work function (Φ), as shown in Equation 1-2.

$$BE = h\nu - KE - \Phi \qquad\qquad (1\text{-}2)$$

The binding energy is characteristic of an element and core energy level. Shifts in binding energy positions, resulting from Coulombic interactions between an emitted photoelectron and the electropositive ion, provide information about the chemical environment.

Auger electron spectroscopy (AES) is a surface analysis technique similar to XPS and is used for elemental identification and depth profiling. The Auger process involves three electrons. An electron beam is directed onto the sample and ionizes core atomic energy levels. After an electron is ejected, a second electron from a higher energy level

relaxes into the vacated lower energy level. The relaxation energy that is released may be transferred to a third electron, known as the Auger electron, with sufficient energy for ejection. The kinetic energy (KE) of the Auger electron is independent of the energy of the incident electron beam, and only depends on the differences in binding energies (BE) of the three electrons involved, as shown in Equation 1-3. The subscripts refer to each of the three electrons in the process.

$$KE_3 = (BE_2 - BE_1) - BE_3 \qquad (1\text{-}3)$$

Spectroscopic ellipsometry (SE) is an optical technique for determining film thickness and optical properties. Linearly polarized light is directed at the sample and reflected into a photodetector. Psi and delta data are collected as a function of incident angle and wavelength and are related to changes in the amplitude and phase, respectively, of the reflected light. Optical models of the sample are generated and fitted to the experimental data. Available fitting parameters include film thickness, void fraction, degree of intermixing, surface roughness, index of refraction, and extinction coefficient.

Capacitance-voltage (C-V) measurements are commonly used to evaluate the electrical properties of films [29]. The dielectric constant and flat band voltage shift indicate how the film behaves under application, but does not provide direct material information.

REFERENCES

1. Barsoum, M.W., *Fundamental of Ceramics*. Series in Materials Science and Engineering, ed. B. Cantor, Goringe M. J. 2003, Bristol, CT: Institute of Physics Publishing.

2. *Front End Processes*, in *The International Technology Roadmap for Semiconductors*. 2007, International SEMATECH: Austin, Texas.

3. Wilk, G.D., R.M. Wallace, and J.M. Anthony, *High-kappa gate dielectrics: Current status and materials properties considerations.* Journal of Applied Physics, 2001. **89**(10): p. 5243-5275.

4. Wallace, R.M. and G. Wilk, *High-kappa gate dielectric materials.* Mrs Bulletin, 2002. **27**(3): p. 192-197.

5. Schwarzkopf, P. and R. Kieffer, *Refractory Hard Metals*. 1953, New York: The Macmillan Company.

6. Fahrenholtz, W.G. and G.E. Hilmas, *NSF-AFOSR Joint Workshop on Future Ultra-high Temperature Materials*. 2004: Arlington, VA.

7. Upadhya, K., J.M. Yang, and W.P. Hoffman, *Materials for ultrahigh temperature structural applications.* American Ceramic Society Bulletin, 1997. **76**(12): p. 51-56.

8. Pierson, H.O., *Handbook of Refractory Carbides and Nitrides*. Materials Science and Process Technology Series. 1996, Westwood, NJ: Noyes Publications.

9. Opeka, M.M., I.G. Talmy, and J.A. Zaykoski, *Oxidation-based materials selection for 2000 degrees C plus hypersonic aerosurfaces: Theoretical considerations and historical experience.* Journal of Materials Science, 2004. **39**(19): p. 5887-5904.

10. Fahrenholtz, W.G., G.E. Hilmas, I.G. Talmy, and J.A. Zaykoski, *Refractory diborides of zirconium and hafnium.* Journal of the American Ceramic Society, 2007. **90**(5): p. 1347-1364.

11.   Shimada, S., F. Yunazar, and S. Otani, *Oxidation of hafnium carbide and titanium carbide single crystals with the formation of carbon at high temperatures and low oxygen pressures.* Journal of the American Ceramic Society, 2000. **83**(4): p. 721-728.

12.   Zhilyaev, V.A., Zainlulin, Yu.G., Alyamovskii, S.I. and G.P. Shveikin, *High-temperature oxidation of zirconium and hafnium oxycarbides, and oxycarbonitrides* Powder Metallurgy and Metal Ceramics, 1972. **11**(8): p. 632-636.

13.   Bargeron, C.B., R.C. Benson, A.N. Jette, and T.E. Phillips, *Oxidation of Hafnium Carbide in the Temperature-Range 1400-Degrees to 2060-Degrees-C.* Journal of the American Ceramic Society, 1993. **76**(4): p. 1040-1046.

14.   Shimada, S., *Interfacial Reaction on Oxidation of Carbides with Formation of Carbon.* Solid State Ionics, 2001. **141-142**: p. 99-104.

15.   Bargeron, C.B., Benson, R.C., and A.N. Jette, *Diffusion of Oxygen in Oxidizing Hafnium Carbide Films at High Temperatures.* Johns Hopkins Apl Technical Digest.

16.   McCullough, J.P., J.F. Messerly, R.T. Moore, and S.S. Todd, *Trimethylaluminum: thermodynamic functions in the solid and liquid states, 0-380°K, vapor pressure, heat of vaporization, and entropy in the ideal gas state.* Journal of Physical Chemistry, 1963. **67**(3): p. 677-679.

17.   Tsubouchi, K. and K. Masu, *Precursor Design and Selective Aluminum Cvd.* Vacuum, 1995. **46**(11): p. 1249-1253.

18.   Jeon, W.S., S. Yang, C.S. Lee, and S.W. Kang, *Atomic layer deposition of Al2O3 thin films using trimethylaluminum and isopropyl alcohol.* Journal of the Electrochemical Society, 2002. **149**(6): p. C306-C310.

19.   Liu, H.N., D.C. Bertolet, and J.W. Rogers, *The Surface-Chemistry of Aluminum Nitride Mocvd on Alumina Using Trimethylaluminum and Ammonia as Precursors.* Surface Science, 1994. **320**(1-2): p. 145-160.

20. Sekiguchi, S., T. Miyamoto, F. Koyama, and K. Iga, *Auto-doping of carbon to AlAs grown by metalorganic chemical vapor deposition using trimethylaluminum and tertiarybutylarsine.* Japanese Journal of Applied Physics Part 1-Regular Papers Short Notes & Review Papers, 1997. **36**(5A): p. 2638-2639.

21. Aboaf, J.A., *Deposition and Properties of Aluminum Oxide Obtained by Pyrolytic Decomposition of an Aluminum Alkoxide.* Journal of the Electrochemical Society, 1967. **114**(9): p. 948-&.

22. Gleizes, A.N., C. Vahlas, M.M. Sovar, D. Samelor, and M.C. Lafont, *CVD-Fabricated aluminum oxide coatings from aluminum tri-iso-propoxide: Correlation between processing conditions and composition.* Chemical Vapor Deposition, 2007. **13**(1): p. 23-29.

23. Bradley, D.C., Mehrotra, R.C., and D.P. Gaur, *Metal Alkoxides.* 1978, London: Academic Press.

24. An, K.S., W.T. Cho, K.H. Sung, S.S. Lee, and Y. Kim, *Preparation of Al2O3 thin films by atomic layer deposition using dimethylaluminum isopropoxide and water and their reaction mechanisms.* Bulletin of the Korean Chemical Society, 2003. **24**(11): p. 1659-1663.

25. Cho, W., K. Sung, K.S. An, S.S. Lee, T.M. Chung, and Y. Kim, *Atomic layer deposition of Al2O3 thin films using dimethylaluminum isopropoxide and water.* Journal of Vacuum Science & Technology A, 2003. **21**(4): p. 1366-1370.

26. Koo, J., S. Kim, S. Jeon, H. Jeon, Y. Kim, and Y. Won, *Characteristics of Al2O3 thin films deposited using dimethylaluminum isopropoxide and trimethylaluminum precursors by the plasma-enhanced atomic-layer deposition method.* Journal of the Korean Physical Society, 2006. **48**(1): p. 131-136.

27. Barreca, D., G.A. Battiston, R. Gerbasi, and E. Tondello, *Al2O3 thin films from aluminium dimethylisopropoxide by metal-organic chemical vapour deposition.* Journal of Materials Chemistry, 2000. **10**(9): p. 2127-2130.

28. Battiston, G.A. and R. Gerbasi, *Aluminum dimethylisopropoxide decomposition and the growth of dense alumina thin films at low temperature.* Chemical Vapor Deposition, 2002. **8**(5): p. 193-195.

29.   Nicollian, E.H. and J.R. Brews, *MOS (metal oxide semiconductor) physics and technology*. 1982, New York: Wiley.

CHAPTER II

METAL-ORGANIC CHEMICAL VAPOR DEPOSITION
OF ALUMINUM OXYCARBIDE THIN FILMS VIA
PYROLYSIS OF DIMETHYLALUMINUM
ISOPROPOXIDE

Introduction

Aluminum oxycarbide films were produced by metal-organic chemical vapor deposition using dimethylaluminum isopropoxide (DMAI) as the precursor. In this chapter, we investigated the relationship between deposition temperature and film composition. Details of the process such as the reaction kinetics and film uniformity are also discussed.

Experimental Details

Description of high vacuum chemical vapor deposition system

A single-wafer warm wall high vacuum CVD reactor was used for all depositions, shown in Figure 2.1. In a warm wall system, the reactor walls are heated to prevent vapor condensation, but the wall temperature is lower than the substrate temperature to prevent deposition reactions at the wall. The pumping system consists of a turbomolecular pump backed by a rotary vane pump. The base pressure of the main chamber was approximately 1×10^{-7} Torr, as measured by a cold cathode ionization gauge. Samples were introduced to the reaction chamber through a load lock chamber pumped by a turbomolecular pump and a rotary vane pump. Wafers were loaded onto a

susceptor with the polished face down. The vertical position of the susceptor assembly
was adjustable.
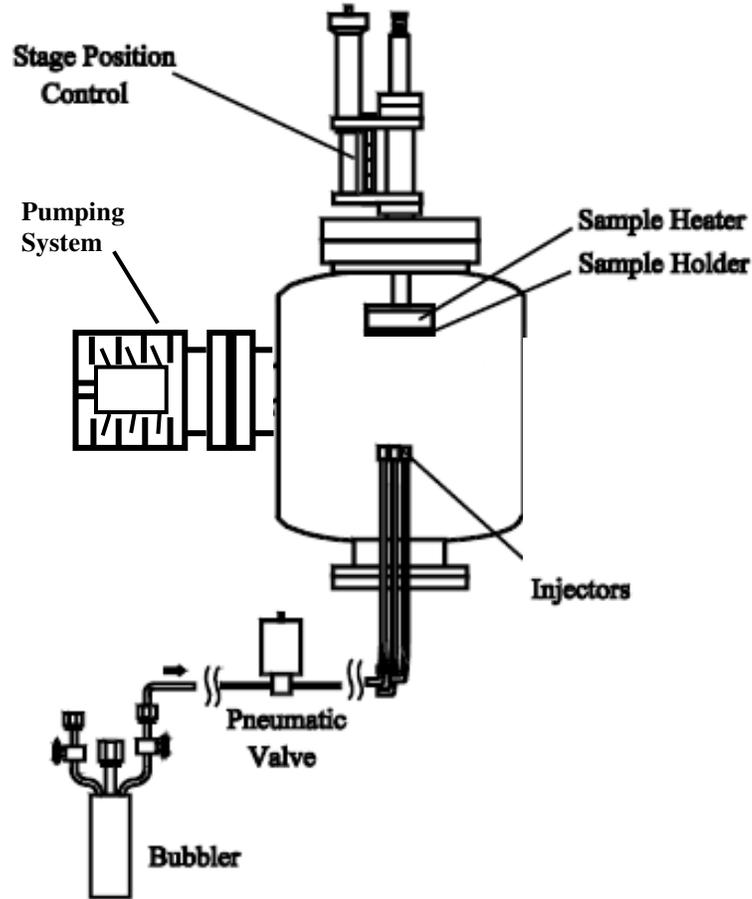
Figure 2.1 – Schematic of chemical vapor deposition system used in this work

Samples were heated radiatively from the back side by a boron nitride-coated
graphite heater approximately 1 cm from the wafer surface. The heater was resistively
heated using a 3kW power supply (Sorenson DCS 150-20). A type-C thermocouple was
embedded near the heated zone and was used in conjunction with the power supply and
Eurotherm 2408 temperature controller to maintain temperature setpoint. A silicon wafer
with five embedded thermocouples (Thermo Electric Company, West Chester, PA, USA)

was used to calibrate wafer temperature to heater setpoint. The chamber walls were heated from the outside by a resistively heated rod, and a thermal insulation blanket was wrapped around the reaction chamber.

Process gases were delivered through a manifold system and introduced into the reactor through injectors at the bottom of the chamber. The CVD precursor was held in a stainless steel bubbler and maintained at temperature in a heated bath. A carrier gas was used to enhance transport of precursor vapors to the reactor. The carrier gas is bubbled through the liquid precursor to increase the surface area of the vapor-liquid interface. The precursor was assumed to evaporate into the bubble up to its vapor pressure. Carrier gas flow rate was controlled by a mass flow controller (MKS, Andover, MA, USA). A pneumatic valve located between the bubbler and injectors actuated flow to the chamber. The gas transfer lines were heated to prevent precursor condensation during transport to the reactor.

In this work, substrate temperatures at the center of the wafer during deposition were 417 – 659 °C. DMAI was delivered from a bubbler held at 40 °C. Ultrahigh purity nitrogen was used as the carrier gas at a flow rate of 5 cm^3/minute at standard temperature and pressure (sccm). DMAI was the only oxygen-containing gas delivered to the reactor. Gas transfer lines between the bubbler and reactor chamber were maintained at 60 °C to prevent precursor condensation. Reactor walls were heated to 150 °C to prevent condensation of vapors. Total reactor pressure during deposition was approximately 1.5 mTorr, with a DMAI partial pressure of approximately 0.5 mTorr, as measured by a capacitance manometer. Samples were exposed to process gases for varied lengths of time based on the desired film thickness.

Synthesis of dimethylaluminum isopropoxide

DMAI was prepared according to literature procedure [2, 3]. A 100 mL Schlenk flask equipped with a magnetic stir bar was charged with isopropyl alcohol (15.0 mL, 0.196 mol). The alcohol was degassed and cooled to -78 °C with a mixture of dry ice and acetone. Trimethylaluminum (14.373 g, 0.1994 mol) was then slowly added to the alcohol over 30 minutes. The reaction rapidly evolved gas, and was allowed to continue 30 minutes after the gas evolution had ceased. The reaction product was a clear, colorless liquid in quantitative yield. The ^{1}H nuclear magnetic resonance spectrum (not shown) was consistent with literature [1].

Substrate preparation

Si(100) wafers were dipped in a 2 vol% HF/deionized water solution for 30 sec to etch the native oxide layer, rinsed with DI water for 120 sec, and blown dry with nitrogen. A hydrogen-terminated silicon surface is formed by this preparation results and is stable against re-oxidation in air for several hours [2].

Film characterization

Crystallinity was determined by x-ray diffraction (Scintag X_1 θ/θ automated powder X-ray diffractometer). A Cu K_α x-ray source was used ($\lambda = 1.5418$ Å).

Film thickness was determined using *ex situ* spectroscopic ellipsometry (J.A. Woollam M-2000D, Lincoln, NE, USA). Psi (Ψ) and delta (Δ) values were collected in the photon energy range of $1.25 - 6.46$ eV at 75° incidence measured from sample normal. Ellipsometry data were analyzed with WVASE32 software [3].

Film elemental composition and elemental bonding states were determined using X-ray photoelectron spectroscopy (PHI Versaprobe XPS Microprobe, Chanhassen, MN, USA). A 25 W monochromatic Al K$_\alpha$ X-ray beam and 100 μm diameter analysis spot were used for all analyses. Surface charge was neutralized by a beam of 1.3 eV electrons in conjunction with a beam of 10 eV Ar$^+$ ions. Photoelectrons were collected at 45° from sample normal. The binding energy scale was calibrated to the Au 4f$_{7/2}$ peak of a clean gold foil at 84.0 eV.

Results and Discussion

Film composition

Figure 2.2 contains an XPS survey spectrum collected from a film deposited at 599 °C. Spectral peak shapes and positions were compared to reference data [4] for elemental identification. Peaks corresponding to aluminum, oxygen, and carbon were observed. Nitrogen, which was used as a carrier gas, was not detected in the spectrum. We expected hydrogen to be present in the film, but hydrogen cannot be detected by XPS. Results from Figure 2.2 suggest that the films deposited in this study were free of contaminants at concentrations above the XPS detection limit (~ 0.1 at.%) and contained only elements that comprise the DMAI precursor.
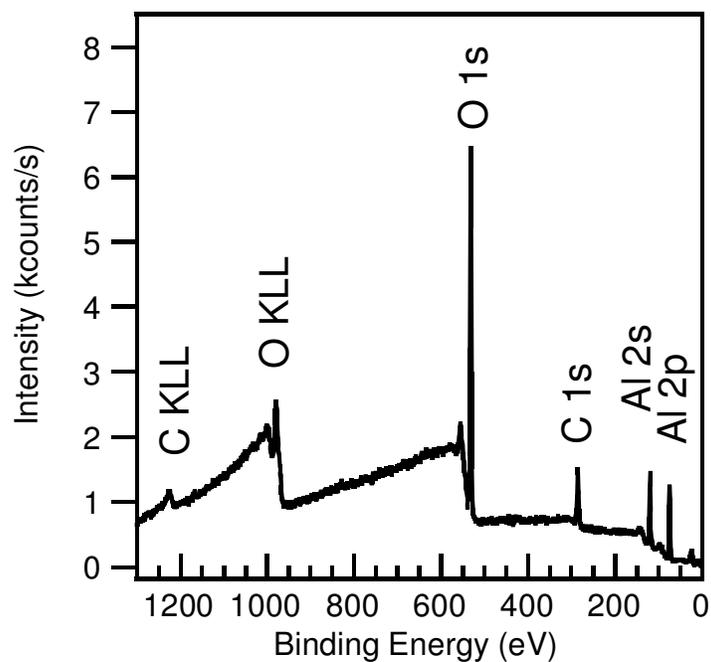
Figure 2.2 - XPS survey spectrum collected from nominally 150 Å thick film deposited on hydrogen-terminated Si(100) at 599 °C.

Figure 2.3 contains high-resolution XPS spectra of the Al 2p and O 1s regions collected from films deposited at 659 and 417 °C, respectively. The binding energies of the peaks in the Al 2p and O 1s regions are 73.9 and 530.6 eV, respectively. These binding energies are in agreement with reported binding energies of Al_2O_3 (74.3 ± 0.6 eV for Al 2p, 530.5 ± 2.2 eV for O 1s) [5].
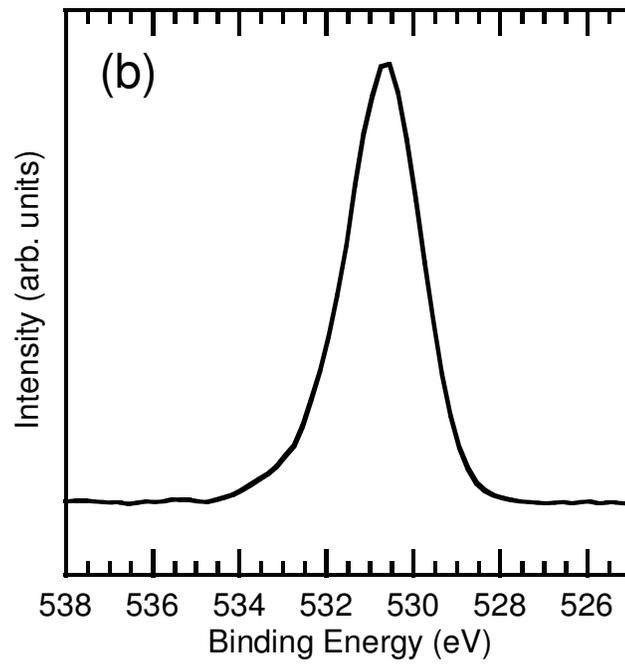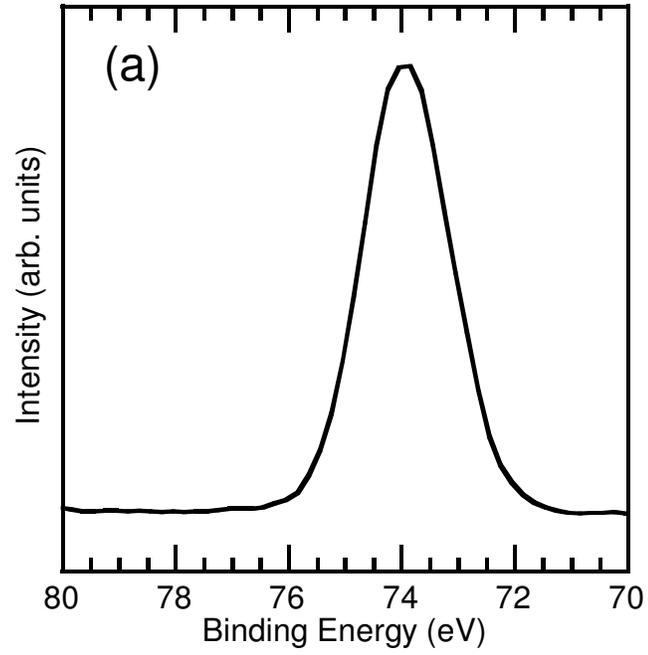
Figure 2.3 – High resolution XPS spectra of: (a) Al 2p region from film deposited at 659 °C (b) O 1s region from film deposited at 417 °C

Figures 2.2 and 2.3 only present information from the surface region of the deposited film. In order to determine the elemental composition deeper into the film, we performed a depth profile by sequentially removing layers of surface atoms and then collecting spectra. We bombarded the surface with a 2 keV argon ion beam in the analysis chamber to remove surface layers. The beam was incident at 55° off sample normal and rastered over a 2 x 2 mm area. Ion current density was determined by collecting charge into a Faraday cup and was 21 $\mu A/cm^2$. The etch rate of SiO_2 under these bombardment conditions was determined by sputtering through a thermal SiO_2 film on silicon. The thickness of the film prior to sputtering was determined using spectroscopic ellipsometry. Under these sputter conditions the etch rate of SiO_2 was 74 Å/min.

Figure 2.4 is the depth profile of a film deposited at 659 °C. The film was sputtered in 30 second increments. After each sputter cycle, high-resolution spectra were collected from the Al 2p, O 1s, C 1s, and Si 2p regions. A Shirley background shape was used, and the peak area intensity of each region was calculated by subtracting the measured intensity from the background. The intensity of each peak was then plotted as a function of sputter time. Aluminum, oxygen, and carbon signals were observed above the background for sputter times less than about 15 minutes. A silicon substrate signal was observed after approximately 12 minutes of sputtering. The etch rate of the film was approximately 45 Å/min.

The depth profile of the film can be described in four regimes. In the first regime (<2 minutes sputter time), the surface of the as-received film was analyzed. The large oxygen and carbon intensities were attributed to adventitious carbonaceous material from

the ambient that adsorbed to the sample surface during transport outside of vacuum. The

second regime (2 – 11 minutes sputter time) contains information from the bulk of the

film. Oxygen, aluminum, and carbon intensities were relatively constant, and suggested

that these elements were uniformly dispersed throughout the bulk region of the film. The

third regime (12 – 15 minutes sputter time) consists of information from the

film/substrate interface. The intensities of the film components all decreased to

background levels, while the intensity of the substrate silicon increased. After 15

minutes of sputter time, the fourth regime shows that only the spectrum collected from

the silicon region had peak intensity greater than the background, and thus suggested that

the film had been completely removed from the analysis area. It should be noted that the

absence of a silicon signal at early sputter times suggested that the film was continuous

and free of pinholes in the analysis area.
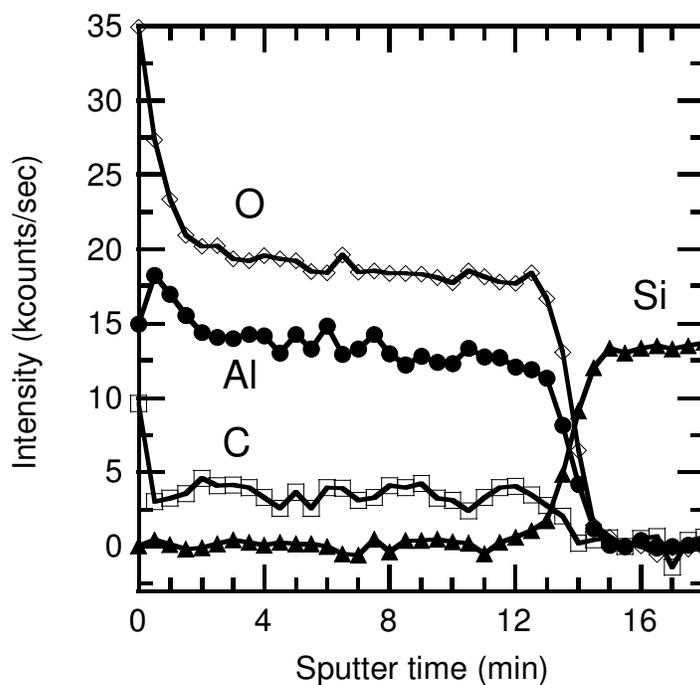
Figure 2.4 - XPS depth profile of nominally 625 Å thick film deposited on silicon at 659 °C. Al 2p, C 1s, O 1s, and Si 2p peak areas are plotted as a function of sputter time. Sputtering was performed in 30 second intervals.

The measured peak intensities were converted to atomic concentrations by applying corrections to the peak areas. Sensitivity factors accounted for variations in signal intensity due to differences in photoionization cross-section (related to the material under investigation). Transmission function corrections accounted for variations in signal intensity due to the efficiency of the photoelectron energy analyzer (related to the analysis equipment). Empirical sensitivity factors were provided by the equipment manufacturer for use with the Versaprobe system [6]. The published sensitivity factors are only valid for system geometries where the angle between the x-ray source and the analyzer is 54.7°. The XPS system used for this study has an angle of 45° between the x-

ray source and source. The sensitivity factors were adjusted within the analysis software to account for asymmetry in the photoionization process [7].

Figure 2.5 is the depth profile presented in Figure 2.4 after calculation of atomic composition at each sputter time. In the bulk film regime, the results in Figure 2.5 suggest that the stoichiometry of the film deposited at 659 °C was approximately $Al_2O_{2.5}C_{0.5}$. The O/Al ratio was 1.25, which is smaller than the O/Al ratio of 1.50 in stoichiometric Al_2O_3.
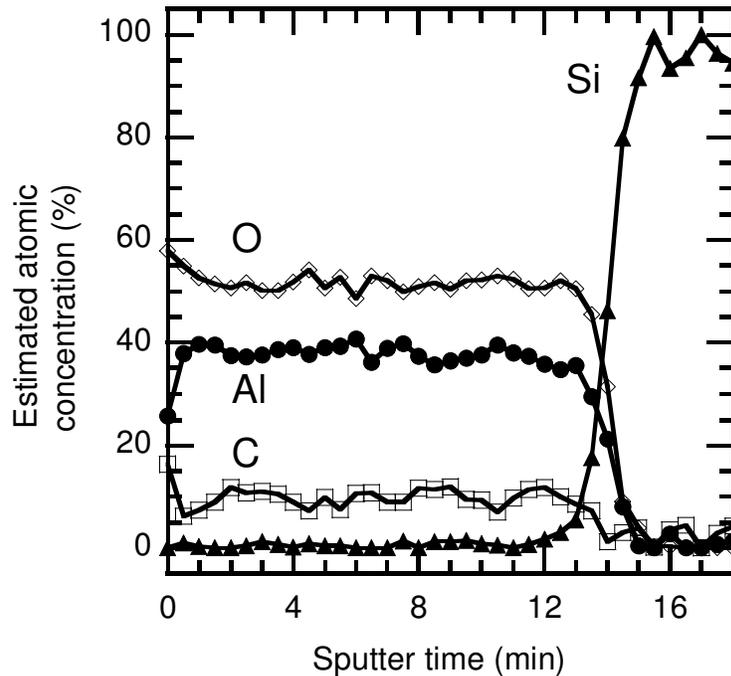
Figure 2.5 - XPS depth profile of nominally 625 Å thick film deposited on silicon at 659 °C. Al 2p, C 1s, O 1s, and Si 2p peak areas have been converted to estimated atomic concentrations using sensitivity factors provided by PHI [6].

The effect of deposition temperature on film carbon content was investigated by XPS. A set of films was produced in the deposition temperature range 417-659 °C. The

films were nominally either 50 or 125 Å thick. Each sample was sputter-cleaned for 30

seconds in the XPS analysis chamber using a 500 eV Ar^+ ion beam. The purpose of the

sputter cleaning was to remove the adventitious carbon material on the sample surface, so

that the spectra collected from the sample was more representative of the bulk of the film

than of the surface. Spectra were collected from the Al 2p, O 1s, and C 1s regions, and

peak intensities were converted to atomic concentration using the methods described

earlier. A thick thermal SiO_2 film was sputtered under similar conditions and the Si 2p,

O 1s, and C 1s regions were analyzed as a reference. Theoretically, the bulk regime of

the thermal oxide film contained no carbon.

Figure 2.6 is a plot of the calculated carbon concentration in the aluminum oxide

films as a function of deposition temperature. In the deposition range 417-659 °C, the

carbon concentration increased with increased deposition temperature, from

approximately 1.5 atomic% at 417 °C to 8 atomic% at 659 °C. A similar trend was

observed in a study of the thermal decomposition of aluminum acetylacetonate [8].

However, our results were contradictory with a previous study of thermal decomposition

of aluminum tri-isopropoxide (ATI) [9]. In the current work, the values of the carbon

percentages for the 50 and 125 Å thick films were within 12% at each deposition

temperature. This was consistent with results shown in Figure 2.5, and suggested that the

carbon content was independent of film thickness in the bulk regime. For comparison, a

peak in the C 1s region was observed in the XPS spectrum collected from the thermal

SiO_2 sample after sputter-cleaning. The calculated carbon content of the thermal SiO_2

after sputter-cleaning was around 1.5 atomic%, similar to the amount of carbon observed

in the aluminum oxide film deposited at 417 °C. Since no carbon was expected in the

SiO$_2$ film, this result suggests that the adventitious carbon was not completely removed

after 30 seconds of sputtering. Therefore, the carbon percentages given in Figure 2.6

may be higher than the actual amount present in the bulk of the film.
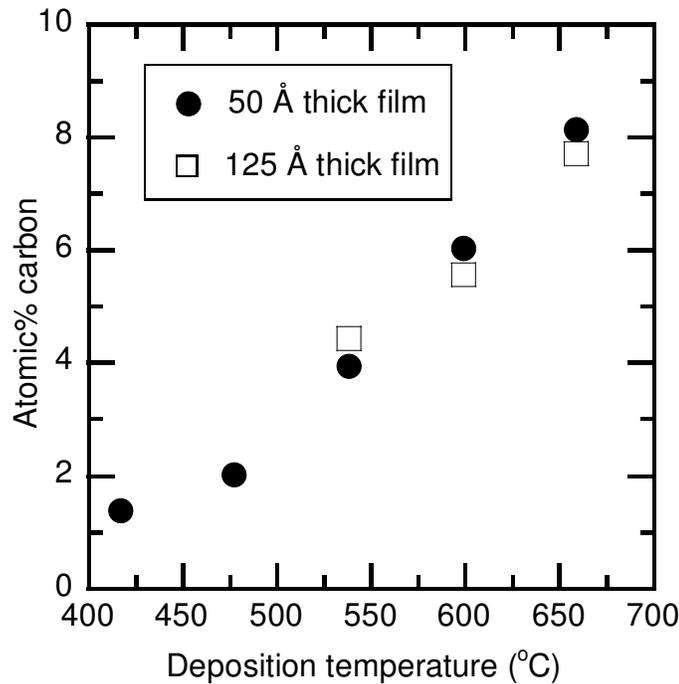
Figure 2.6 - Carbon composition in near-surface region of aluminum oxide film deposited on H-terminated silicon substrate, as a function of substrate temperature and nominal film thickness. Results obtained from high resolution XPS. Quantification was achieved by adjusting peak area in C 1s region with by sensitivity factors. Films were sputter-cleaned under vacuum for 30 seconds using Ar$^+$ ion beam.

Deposition kinetics

Pre-deposition and post-deposition values of psi ($\mathit{\Psi}$) and delta ($\mathit{\Delta}$) were collected

from each sample by ellipsometry. An optical model was used to generate data to

attempt to reproduce experimental psi and delta values at each wavelength. The model

consisted of a single layer on a substrate. The refractive index (*n*) and extinction

coefficient (k) of the substrate were calculated directly from pre-deposition ellipsometry data using Equation 2-1, where φ is the photon incident angle and ρ is related to Ψ and $\varDelta$ as shown in Equation 2-2.

$$n + ik = \sin\varphi\sqrt{1 + \tan^2\varphi\left(\frac{1-\rho}{1+\rho}\right)^2} \qquad (2\text{-}1)$$

$$\rho = \tan\Psi e^{i\Delta} \qquad (2\text{-}2)$$

A Cauchy dispersion model (Equations 2-3 and 2-4) was used to describe the optical properties of the deposited films, where λ is the photon wavelength in units of micrometers. *A* and *B* are parameters to fit curvature of the index function. The Cauchy model is used to describe the optical properties of dielectrics and other materials where a portion of the optical spectrum is non-absorbing [10].

$$n(\lambda) = A + \frac{B}{\lambda^2} \qquad (2\text{-}3)$$

$$k(\lambda) = 0 \qquad (2\text{-}4)$$

Bulk alumina (sapphire) is optically transparent in the approximate range of 150-3700 nm (0.33-8.47 eV) [11]. We assumed that our films were not transparent over the entire spectral range of our ellipsometer due to the presence of carbon impurities. We assumed that the film was transparent at visible wavelengths approaching the IR range and that any absorptions would occur nearer the UV range. In order to use the Cauchy model, we determined that a portion of the spectral range was transparent by plotting the

fit error as a function of the spectral range used for fitting. Mean squared error (MSE) is the figure of merit used to determine goodness of a model fit, and is minimized in the fitting process. The upper bound of the fitting spectral range was set at 995 nm. The lower bound was arbitrarily chosen, and then film thickness and Cauchy parameters were fitted. The MSE value was normalized by the wavelength fitting range. Figure 2.7 shows that the calculated film thickness decreased as the wavelength fitting range was increased (i.e. the wavelength of the lower bound decreased). The normalized MSE exhibited a minimum when the lower wavelength bound was 550 nm. There was a large increase in MSE for lower bounds less than 550 nm. This observation suggested that the Cauchy model could not describe the index function while fitting data outside of the 550-995 nm spectral range, and could also indicate the onset of optical absorption. Therefore, the data fitting range was restricted to 550-995 nm (1.25-2.25 eV) for analysis of all films in this study.
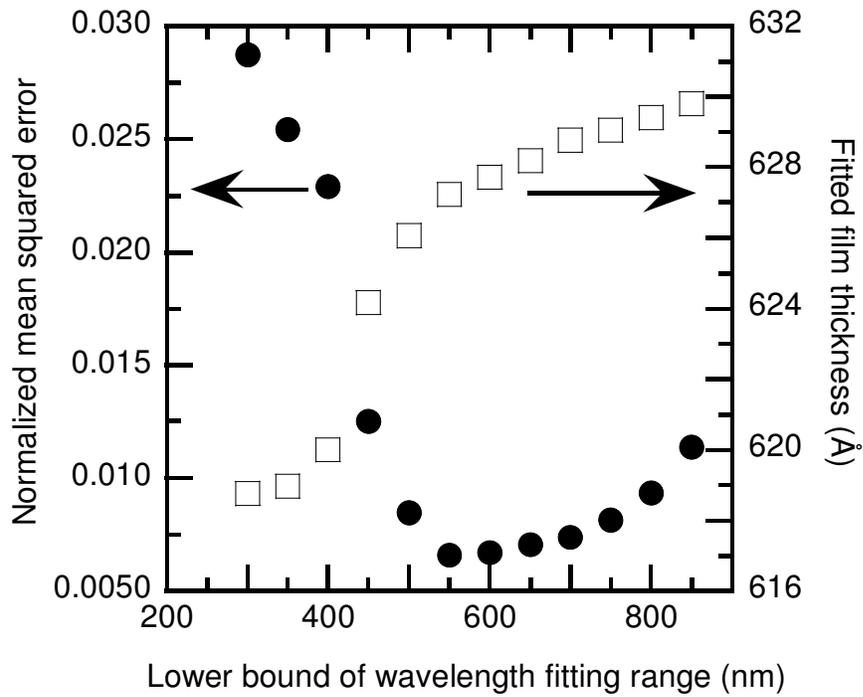
Figure 2.7 - Effect of ellipsometry model fitting range on fitting error. AlO_xC_y film was deposited on silicon at 659 °C. Upper bound of wavelength fitting range was 995 nm. Mean squared error was normalized by wavelength range used for model fitting.

Figure 2.8 contains example ellipsometry data obtained from a nominally 625 Å thick film deposited at 659 °C. Experimental data are displayed as symbols and model-generated data are shown as solid lines. There was good agreement between the experimental and modeled data in the fitting range.
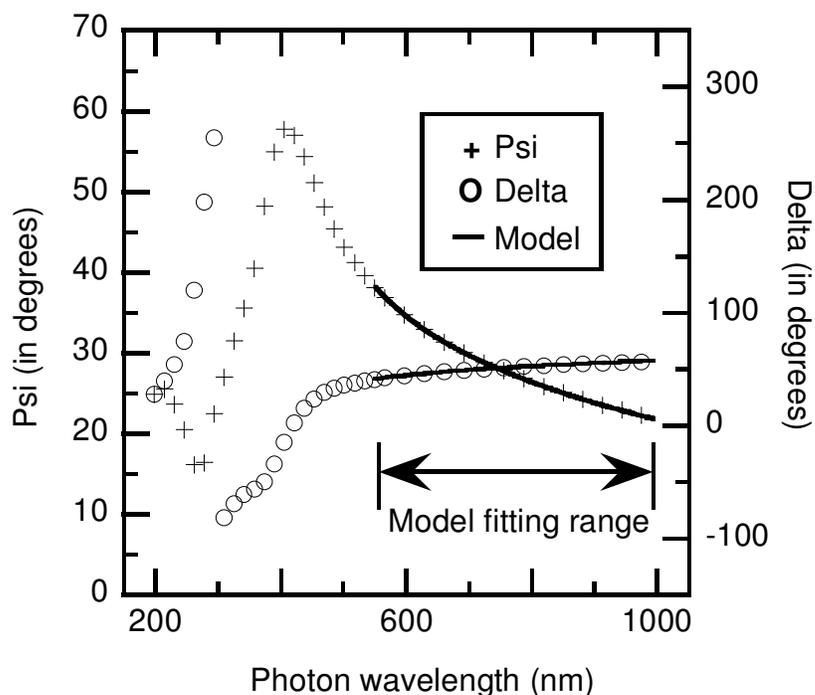
Figure 2.8 - Experimental (symbols) and modeled (lines) psi and delta values collected from a nominally 625 Å thick film deposited at 659 °C on silicon. Optical properties of film were represented by a Cauchy model. Optical properties of the substrate were obtained from analysis prior to deposition. Model fitting wavelength range was 550-995 nm.

The index of refraction of the films at 632.8 nm (1.96 eV) is plotted for films deposited at temperatures between 538 and 659 °C in Figure 2.9. The index was extracted from Equation 2-3 after the film thickness and Cauchy parameters were determined. The index increased with both increased thickness and increased deposition temperature. Refractive index values of 1.65-1.69 for nominally 125 Å thick films were in agreement with MOCVD aluminum oxide films produced from ATI and trimethylaluminum (TMA) [12, 13]. For comparison, reported index values in the Al-C-O system are: sapphire (Al_2O_3), 1.767 at 620 nm [11]; AlO_xC_y thin films, 1.6-2.5 at 632.8 nm [14]; aluminum carbide (Al_4C_3), 2.7 at 632.8 nm [15]. The refractive index of

the nominally 625 Å thick film deposited at 659 °C suggests that there is some aluminum carbide character in the film in addition to the aluminum oxide character. This will be discussed further in Chapter III.

The observation of increased refractive index with increased film thickness was attributed to film densification during the deposition [16]. XPS analysis (not shown) of films deposited at 659 °C indicated no differences in elemental composition or chemical bonding as a function of film thickness even though the refractive index varied from 1.69 to 1.86. To verify our assumption that changes in refractive index were due to densification, a nominally 125 Å thick film deposited at 599 °C was annealed under vacuum at 599 °C so that the total heating time was similar to that of the nominally 350 Å thick film deposited at 599 °C. After annealing, the film index of refraction increased and thickness decreased from the pre-annealing values, which supported our hypothesis that thicker films densified due to increased heating times.
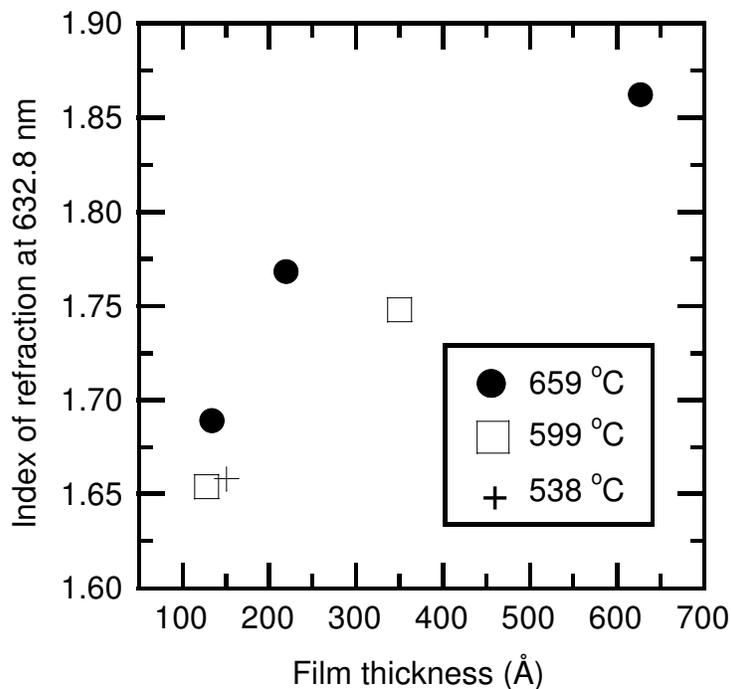
Figure 2.9 - Index of refraction (632.8 nm) of films deposited by thermal decomposition of DMAI on silicon, determined by spectroscopic ellipsometry. Refractive index derived from Cauchy model (Equation 2-3). Data are plotted as functions of film thickness and deposition temperature.

It is difficult to accurately fit both thickness and Cauchy parameters for films thinner than approximately 100 Å because parameter correlations can lead to non-unique solutions [10]. To solve the correlation problem we assumed that that the optical properties of sub-100 Å thick films were similar to the optical properties of nominally 125 Å thick films produced under the same deposition conditions. Thus, to determine the thickness of sub-100 Å thick films we assumed that the refractive index was 1.65 at 632.8 nm. The Cauchy parameters were set as A=1.625 and B=0.01 μm^2, and then used thickness as the only fitting parameter.

Film deposition rate was calculated by measuring film thickness and dividing by the deposition time. We assumed that the deposition rate did not change with time during

the process and that initial deposition effects were negligible. Film thickness was determined by *ex situ* spectroscopic ellipsometry. Deposition time was defined as the amount of time that the precursor bubbler was open. Figure 2.10 displays the deposition rate versus deposition temperature. Deposition rates ranged from approximately 0.2-10 Å/min and the rate increased with increased deposition temperature. Film growth was attained at all deposition temperatures investigated in this study. This observation is in agreement with previous reports indicating that DMAI decomposition begins around 400 °C [17, 18]. No powder particles were observed in the reaction chamber or on the sample surface, which suggested that there was no gas phase reaction and that precursor decomposition occurred only at the substrate surface.
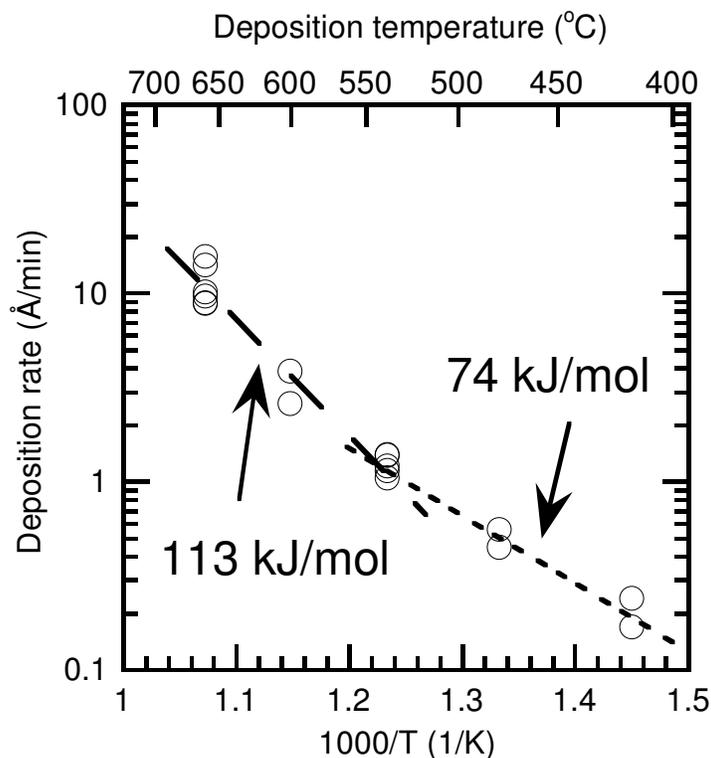
Figure 2.10 – Deposition rate of film produced from pyrolysis of DMAI on silicon. Macroscale activation energy of deposition process is denoted on figure and was derived from least-squares fitting of data to Arrhenius model. Different values of activation energy were determined for 417 – 538 °C (short dash) and 538 – 659 °C (long dash) deposition temperature ranges.

There were two temperature regimes (417 – 538 °C, 538 – 659 °C) in which the deposition rate appeared linear when plotted on a semi-logarithmic scale against reciprocal deposition temperature. This observation suggested the deposition process was limited by the rate of reactions at the surface rather than rate of precursor transport to the surface. The macroscale apparent activation energy of the deposition process for each temperature regime was extracted from the data by manipulating the Arrhenius equation (Equation 2-5) into a form where slope of the linearly-related data contains the apparent activation energy, E_a (Equation 2-6). In the equations, k` is the deposition rate, $A$` is the pre-exponential factor, R is the universal gas constant, and T is the deposition

temperature. The extracted activation energies were 74 and 113 kJ/mol for the 417 – 538 °C and 538 – 659 °C deposition temperature regimes, respectively. The observation of two linear regimes which have different slopes suggests that the deposition mechanism was different between the two deposition temperature ranges in this study.

$$k` = A`e^{-\frac{E_a}{RT}} \tag{2-5}$$

$$\ln(k`) = \ln(A`) + \left(\frac{-E_a}{R}\right)\left(\frac{1}{T}\right) \tag{2-6}$$

As mentioned earlier, we assumed that the refractive index of sub-100 Å thick films was 1.65 at 632.8 nm in order to fit the thickness while avoiding correlation issues. Films deposited at 417 and 477 °C were generally less than 100 Å thick due to the low deposition rate. We investigated the sensitivity of E_a to our assumption of refractive index. We assumed index values in the range of 1.53-1.76 for sub-100 Å thick films and then determined E_a. The activation energy varied within ~1 kJ/mol, suggesting that E_a was insensitive to our assumption.

Apparent activation energies derived from previous studies of MOCVD aluminum oxide films are given in Table 2.1. The activation energy appears to be correlated to the nature of the co-reactant used in the deposition process. The lowest activation energy was reported in a study that employed H_2O as the co-reactant. Processes involving O_2 exhibited higher activation energies than the deposition using water. Battiston [19] performed reactions of DMAI in O_2 or H_2O/O_2 environments and analyzed the composition of exhaust gases. Methane was observed as a byproduct in each case. However, isopropanol was detected as a major byproduct in a water-

containing atmosphere while acetone was observed in the oxygen-only atmosphere. No attempt was made to determine the composition of exhaust gases in this work as a means of identifying prominent reaction mechanisms. It is also difficult to directly compare values of E_a reported in previous work to the values calculated in this work due to differences in experimental systems and the understanding that E_a is not indicative of a specific reaction but rather a combination of processes occurring at the surface.

Table 2.1. Apparent activation energies (E_a) observed in CVD aluminum oxide processes

Aluminum precursor[a]	Co-reactant	Deposition temperature (K)	E_a (kJ/mol)	Reference
ATI	None	523 – 623	76	[20]
ATI	None	523 – 634	98	[21]
ATI	O_2	535 – 634	114	[21]
DMAI	H_2O	473	45	[22]
DMAI	O_2	813 – 873	130	[17]
DMAI	None	690 – 811	74	This work
DMAI	None	811 – 932	113	This work

[a] ATI = aluminum tri-isopropoxide, DMAI = dimethylaluminum isopropoxide

Crystallinity

Figure 2.11 contains x-ray diffraction (XRD) spectra collected from an H-terminated Si (100) wafer before and after deposition of a nominally 625 Å thick film at 659 °C. Each spectrum contains several large peaks. However, the spectrum collected from the sample with the film contains only the peaks that were present in the spectrum collected from the bare substrate. The lack of diffraction peaks due to the film suggests that the deposited film was amorphous.
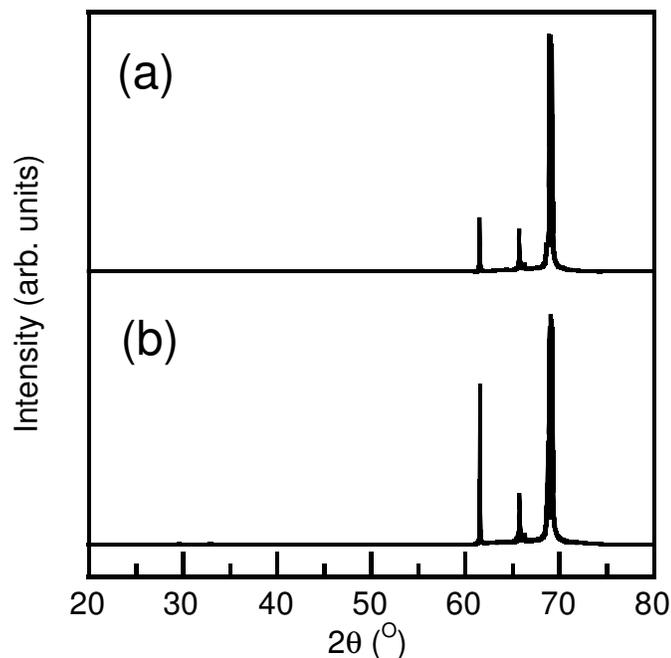
Figure 2.11 – XRD spectra of: (a) 625 Å thick AlO_xC_y film deposited on hydrogen-terminated silicon (100) at 659 °C by thermal decomposition of DMAI, (b) Hydrogen-terminated silicon (100).

Table 2.2 provides diffraction peak positions for several phases observed in the Al-O-C system. Several authors report that alumina films deposited from ATI remained amorphous up to approximately 800 °C [12]. Duffy and Kern [12] reported that films produced from TMA in an oxygen-poor environment (O/Al = 0.1) were predominantly polycrystalline, but films produced in an oxygen-rich environment (O/Al = 2) were amorphous at 800 °C. The film that was analyzed in order to produce Figure 2.11 was the thickest film in this study and was also deposited at the highest temperature in this study. The other films produced in this work were thinner and deposited at lower temperatures. All films in this study were assumed to be amorphous since there was no indication of film crystallinity in the sample described in Figure 2.11.

Table 2.2. XRD peaks observed in Al-O-C system

Phase	Major peak positions (2θ)			JCPDS[a] No. [23]
α-Al$_2$O$_3$ (corundum)	35.152	57.496	43.355	46-1212
γ-Al$_2$O$_3$	45.827	67.367	37.311	47-1308
Al$_2$OC	32.559	35.336	58.205	36-0148
Al$_4$C$_3$	31.740	55.043	40.075	35-0799

[a] Joint Committee on Powder Diffraction Standards, also known as International Centre for Diffraction Data (ICDD)

Thickness and composition uniformity

In the previous discussion on film thickness and deposition rate, measurements were only collected at the center of the wafer. To determine film thickness uniformity across a single wafer, we calculated thickness at several locations for comparison. Figure 2.12 shows film thickness across the 3-inch diameter wafer for a film deposited at 599 °C. Film thicknesses were determined at the wafer center and four points approximately 25 mm from the wafer center and 90° apart. Table 2.3 describes the locations designated on the wafer. The film was thickest at the center and thinner near the edges. Thickness gradients from the center to the edge varied depending on direction.
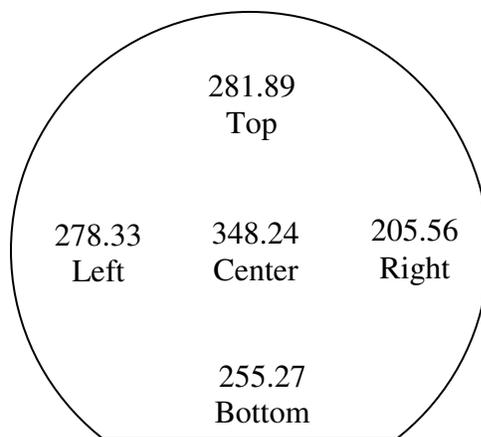
Figure 2.12 - Thickness of film (in Angstroms) at various locations across 3-inch wafer. The deposition temperature was 599 °C. Edge measurements were performed approximately 25 mm from wafer center.

Table 2.3. Descriptions of wafer location in Figure 2.12

Label on Figure 2.12	Wafer location[a]
Center	Center
Left	Beneath heater power supply (-V)
Right	Beneath heater power supply (+V)
Top	Towards turbo pump
Bottom	Away from turbo pump

[a] Off-center locations are 25 mm from center. A line connecting each off-center location to the center lies parallel or perpendicular to the wafer flat.

Film thickness nonuniformities may be related to either transport or thermal effects in the reaction zone. The characterizations of the gas flows in the chamber during depositions and the thermal profiles of the substrate are presented in the following sections.

Bulk gas transport in the reactor was classified based on the probability of

molecule-molecule (viscous flow) versus molecule-wall (molecular flow) interactions. In

a molecular flow regime, particle trajectories are random, and theoretically should be

well-mixed within the reactor. However, in viscous flow there are distinct streamlines,

and there may be concentration gradients and dead space based on the reactor geometry.

The dimensionless Knudsen number (N_{Kn}) was used to determine the flow regime, and

was calculated by comparing the mean free path (λ_{mfp}) of a molecule to the characteristic

dimensions of the container (L), as shown in Equation 2-7.

$$N_{Kn} = \frac{\lambda_{mfp}}{L} \qquad (2\text{-}7)$$

The relationship between Knudsen number and flow regime is shown below:

$N_{Kn} > 0.5$ Molecular flow regime

$10^{-2} < N_{Kn} < 0.5$ Transition regime

$N_{Kn} < 10^{-2}$ Viscous flow regime

The mean free path is the average distance a molecule will travel between elastic

collisions, and was determined from Equation 2-8, where k_B is Boltzmann's constant, T is

temperature, d is the molecular diameter, and p is the pressure.

$$\lambda_{mfp} = \frac{k_B T}{\sqrt{2}\pi d^2 p} \qquad (2\text{-}8)$$

As a generic example based on our deposition conditions, the mean free path of a nitrogen molecule ($d \sim 3$ Å) at a pressure of 1.5 mTorr and temperature of 150 °C is approximately 7 cm. The reactor diameter was 30 cm, and thus the calculated Knudsen number was 0.23, which is in the transition flow regime. Under actual deposition conditions, the gas temperature will be some intermediate value between the wall temperature and the heater temperature due to radiative heating, resulting in an increase in N_{Kn}. DMAI normally exists as a dimer in the gas phase [18] and is much larger than a nitrogen molecule, and thus will decrease the average mean free path in the chamber, and hence will decrease N_{Kn}. Based on the temperature and molecular size considerations, the flow in the chamber was assumed to be either viscous or in the transition regime, but never fully molecular flow.

Substrate temperatures across the wafer were determined by using a 3-inch silicon wafer with type-K thermocouples embedded into the surface (Thermo Electric Company Inc., West Chester, PA). Five thermocouples were embedded in the wafer in positions similar to those shown in Figure 2.12, and the edge probes were each 25 mm from the center probe. The thermocouple leads were attached to an electrical feedthrough mounted on the vacuum chamber. A digital display was attached to the air-side feedthroughs for readout of the temperature. To simulate process conditions, the thermocouple wafer was loaded in the reactor in the same orientation used during depositions. The reactor walls were maintained at 150 °C, the system pressure was less than 10^{-4} torr, and there was no gas flow.

The relationship between center and edge temperatures is provided in Table 2.4. For center temperatures (T_c) $\leq$ 289 °C, the temperature variation across the wafer was

less than 1%. The difference between T_c and edge temperatures increased as T_c increased above 358 °C. At T_c = 592 °C, the average of the edge temperatures was 5.2% below T_c, but the individual edge temperatures were within 2.3% of each other.

Table 2.4. Location – specific substrate temperature (°C)

Center	Top	Left	Bottom	Right
26	26	26	26	26
124	123	123	123	124
152	155	155	156	153
289	287	288	287	288
358	352	352	351	351
422	412	411	411	409
484	469	467	468	463
540	519	516	519	510
592	564	561	567	554
660[a]	531[b]	604	608	569

[a] Thermocouple signal erratic. Temperature extrapolated from calibration curve of center temperature versus setpoint temperature in the 300-550 °C temperature range.
[b] Thermocouple signal erratic.

Figure 2.13 shows the deposition rate data from Figure 2.10 (dark symbols), but also contains the deposition rate calculated at each of the wafer positions for the sample shown in Figure 2.12 (open symbols), where the plotted deposition temperature was determined from Table 2.4. The data points are collinear with the data points of deposition rate calculated at the center of the sample, suggesting that the deposition rate at non-center positions is also in the kinetic-limited regime.
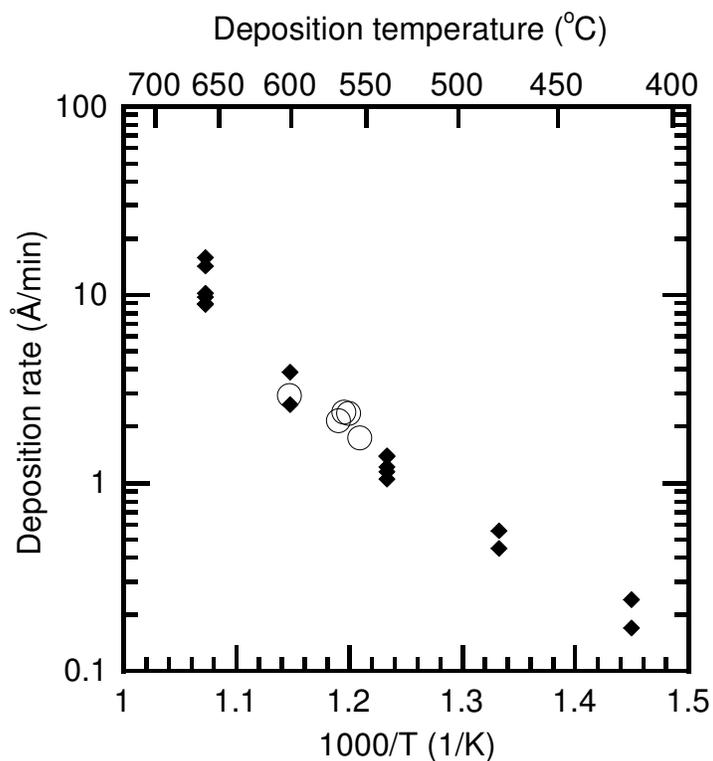
Figure 2.13 - Film deposition rate versus substrate temperature. Open circles correspond to deposition rates determined at locations given in Figure 2.12.

Based on the discussion of Figure 2.10, the deposition rate at the center of the wafer was limited by the surface reaction rate. Under a kinetically-controlled reaction regime where other parameters remain fixed, the reaction rate is determined by the surface temperature. Therefore, the variation in deposition rate across the substrate was attributed to the variation of the substrate temperature during the deposition process.

Conclusions

Aluminum oxycarbide (AlO_xC_y) films were deposited on silicon substrates in the 417 – 659 °C temperature range via pyrolysis of dimethylaluminum isopropoxide precursor. At the described process conditions, the deposition was kinetically-limited.

The apparent activation energy of the deposition process was larger in the 538 – 659 °C deposition temperature range than in the 417 – 538 °C temperature range, which suggested a change in the deposition mechanism as a function of substrate temperature. Thickness nonuniformity was attributed to a nonuniform substrate temperature profile.

Carbon content within the films increased with increased deposition temperature. However, the composition of the films was not representative of the precursor. The Al:O:C atomic ratio in the DMAI molecule is 1:1:5. We observed that the O/Al was greater than one and the concentration of carbon was roughly 10 at.% in films deposited at 659 °C. Carbon distribution and bonding within the film is the focus of Chapter III.

REFERENCES

1.   Rogers, J.H., A.W. Apblett, W.M. Cleaver, A.N. Tyler, and A.R. Barron, *Dimethylaluminum Alkoxides - a Physicochemical Investigation.* Journal of the Chemical Society-Dalton Transactions, 1992(22): p. 3179-3187.

2.   Pawar, V.D., *Study of native oxide etching, kinetics of native oxide growth and surface termination in p-type Si (100) substrates*, in *Interdisciplinary Materials Science*. 2002, Vanderbilt University: Nashville, TN.

3.   Johs, B., C. Herzinger, and B. Guenther, *WVASE32*. 2003, J. A. Woollam Co.: Lincoln, NE.

4.   John F. Moulder, W.F.S., Peter E. Sobol, Kenneth D. Bomben, *Handbook of X-ray photoelectron spectroscopy*, ed. R.C.K. Jill Chastain, Jr. 1995, Chanhassen, Minnesota: Physical Electronics USA, Inc.

5.   *NIST X-ray Photoelectron Spectroscopy Database*.   [cited 2007 February 14]; Available from: http://srdata.nist.gov/xps.

6.   Ulvac-PHI, Inc., *Operator's PHI Multipak software manual, version 8.2C*. 2007, Chigasaki City, Kanagawa Prefecture, Japan: Ulvac-PHI, Inc.

7.   Fairley, N. and A. Carrick, *The Casa Cookbook, Part 1: Recipes for XPS data processing*. 2005, Cheshire, U.K.: Acolyte Science.

8.   Maruyama, T. and S. Arai, *Aluminum-Oxide Thin-Films Prepared by Chemical Vapor-Deposition from Aluminum Acetylacetonate.* Applied Physics Letters, 1992. **60**(3): p. 322-323.

9.   Gleizes, A.N., C. Vahlas, M.M. Sovar, D. Samelor, and M.C. Lafont, *CVD-Fabricated aluminum oxide coatings from aluminum tri-iso-propoxide: Correlation between processing conditions and composition.* Chemical Vapor Deposition, 2007. **13**(1): p. 23-29.

10.   Tompkins, H.G. and W.A. McGahan, *Spectroscopic ellipsometry and reflectometry : a user's guide*. 1999, New York: Wiley. xiv, 228 p.

11. Tropf, W.J. and M.E. Thomas, *Handbook of Optical Constants of Solids*, ed. E.D. Palik. Vol. 2. 1998, New York: Academic Press.

12. Duffy, M.T. and W. Kern, *Chemical vapor deposition of aluminum oxide films from organo-aluminum compounds.* RCA Review, 1970. **31**: p. 754-770.

13. Aboaf, J.A., *Deposition and Properties of Aluminum Oxide Obtained by Pyrolytic Decomposition of an Aluminum Alkoxide.* Journal of the Electrochemical Society, 1967. **114**(9): p. 948-&.

14. Zhiqiang, Y. and G.L. Harding, *Optical properties of d.c. reactively sputtered thin films.* Thin Solid Films, 1984. **120**(2): p. 81-108.

15. Gaertner Scientific.   [cited 2009 September 16]; Available from: http://mmrc.caltech.edu/Ellipsometer/Gaertner%20Ellipsometer%20Manual.pdf.

16. Jerman, M., Z.H. Qiao, and D. Mergel, *Refractive index of thin films of SiO2, ZrO2, and HfO2 as a function of the films' mass density.* Applied Optics, 2005. **44**(15): p. 3006-3012.

17. Barreca, D., G.A. Battiston, R. Gerbasi, and E. Tondello, *Al2O3 thin films from aluminium dimethylisopropoxide by metal-organic chemical vapour deposition.* Journal of Materials Chemistry, 2000. **10**(9): p. 2127-2130.

18. Lee, S.Y., B. Luo, Y.M. Sun, J.M. White, and Y.S. Kim, *Thermal decomposition of dimethylaluminum isopropoxide on Si(100).* Applied Surface Science, 2004. **222**(1-4): p. 234-242.

19. Barreca, D., G.A. Battiston, G. Carta, R. Gerbasi, G. Rossetto, E. Tondello, and P. Zanella, *Al2O3 growth optimisation using aluminium dimethylisopropoxide as precursor as a function of reaction conditions and reacting gases.* Journal De Physique Iv, 2001. **11**(Pr3): p. 539-546.

20. Saraie, J., Kwon, J., and Y. Yodogawa, *Chemical Vapor Deposition of Al2O3 Thin Films under Reduced Pressures.* Journal of the Electrochemical Society, 1985. **132**(4): p. 890-892.

21.	Go, T., N. Hara, and K. Sugimoto, *In-Situ Ellipsometric Analysis of Formation Process of Al2o3 Thin-Films in Low-Pressure Cvd.* Journal of the Japan Institute of Metals, 1993. **57**(9): p. 1041-1046.

22.	Battiston, G.A. and R. Gerbasi, *Aluminum dimethylisopropoxide decomposition and the growth of dense alumina thin films at low temperature.* Chemical Vapor Deposition, 2002. **8**(5): p. 193-195.

23.	International Centre for Diffraction Data, *PCPDFWIN*. 1997.

CHAPTER III

ANALYSIS OF CARBON IMPURITIES WITHIN
MOCVD ALUMINUM OXIDE FILMS

Introduction

In Chapter II, aluminum oxide thin films were deposited by MOCVD of
dimethylaluminum isopropoxide (DMAI). Macroscopic details such as film composition
and deposition kinetics were determined. The films contained carbon as an impurity, and
the concentration increased with increasing deposition temperature.

In this chapter, the carbon impurities in the film were investigated in greater
detail. Depth profiles were collected using destructive and non-destructive techniques to
determine both location and bonding environments of the carbon in the films. Synthetic
peaks were fitted to XPS spectra to understand the chemical bonding in the films. We
summarize the observations of the stoichiometry of the films, and compare our results to
previous studies of pyrolysis of DMAI in order to explain our observations.

Experimental Details

Film deposition

Films were deposited from DMAI in a HV-CVD reactor described in detail in
Chapter II. Three inch diameter Si (100) substrates were used. Substrates were cleaned
in a 2 vol% HF/deionized water (DI) solution for 90 sec, rinsed with DI water for 120

sec, and blown dry with nitrogen. This substrate preparation leads to a hydrogen-terminated Si surface [1].

Substrate temperature during deposition ranged from 417 to 659 °C. The DMAI was delivered from a bubbler held at 40 °C using ultrahigh purity nitrogen at a flow rate of 5 sccm as a carrier gas. Gas transfer lines between the bubbler and reactor chamber were maintained at 60 °C. Total reactor pressure during deposition was approximately 1.5 mTorr, with a DMAI partial pressure of approximately 0.5 mTorr.

Film Characterization

Film thickness was determined using spectroscopic ellipsometry (J.A. Woollam M-2000D, Lincoln, NE, USA). A two-layer optical model was fitted to psi and delta values collected at a 75° incident angle in the photon energy range of 1.2 – 6.5 eV. The optical constants of the prepared substrates were collected prior to deposition, and a Cauchy dispersion layer was used to model the deposited film.

Film elemental composition and bonding were determined using X-ray photoelectron spectroscopy (Physical Electronics PHI 5000 Versaprobe, Chanhassen, MN, USA). All analyses were performed using a 50 W monochromatic Al Kα X-ray beam (1486.6 eV) and a 200 µm spot size. Photoelectrons were collected into a spherical capacitor analyzer with pass energies of 187.85 or 23.50 eV for survey or high-resolution spectra, respectively. Surface charge calibration was achieved by setting the binding energy of the peak in the C 1s region that corresponds to C-C bonding to 284.8 eV [2]. XPS data analyses were performed using the commercially available CasaXPS software

[3]. A Shirley background with Gaussian-Lorentzian product line shapes and a

Marquardt fitting algorithm were used for peak fitting.

Elemental depth profiling was achieved using a cylindrical mirror analyzer-based,

fixed beam Auger electron spectroscopy (AES) system. A 2 keV primary electron beam

(45 µA/cm^2 into an unbiased Faraday cup) incident at 10° off sample normal was used.

A 1 keV Ar$^+$ ion beam incident at 65° off sample normal was used for depth profiling

(13.6 µA/cm^2). AES data were analyzed using the CasaXPS [3] software. Peak-to-peak

heights of the Al *LMM* (70 eV), Si *LMM* (90 eV), C *KLL* (278 eV) and O *KLL* (510 eV)

peaks were collected and normalized using sensitivity factors provided by Physical

Electronics [4]. Since sensitivity factors for 1 keV primary electrons are not published,

the sensitivity factors for 3 keV primary electrons were used.

Results and Discussion

Distribution of carbon within films

In Figure 3.1 below, the calculated atomic fraction of carbon in the deposited film

was compared to the calculated atomic fraction of aluminum in the film. The C/Al ratio

is plotted against deposition temperature. The data in Figure 3.1 was determined from

XPS analysis, and is an extension of Figure 2.6. The C/Al ratio increased with increased

deposition temperature. The ratio was much less than the ratio of carbon to aluminum in

DMAI (C/Al = 5). This observation will be discussed later in the chapter.
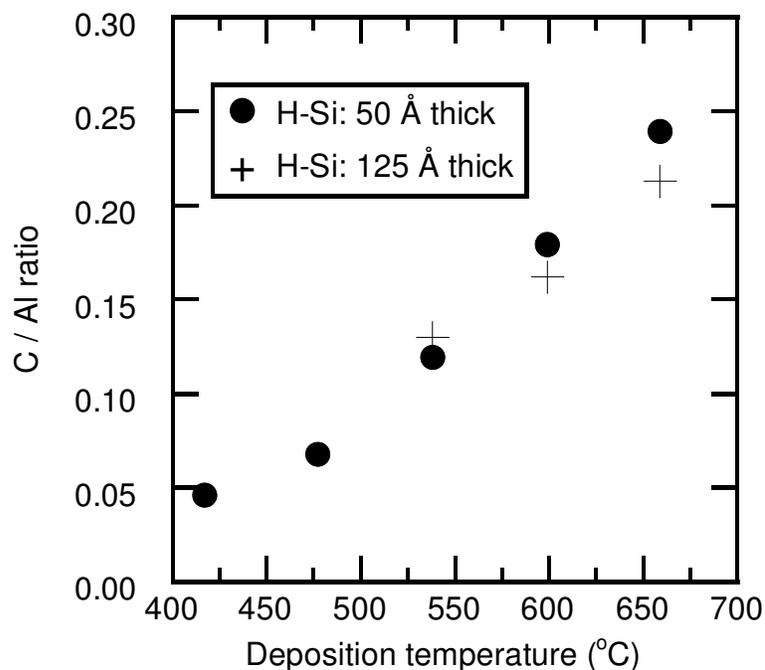
Figure 3.1 – Carbon/aluminum ratio in films deposited from thermal decomposition of DMAI, as calculated by XPS. Films were sputter cleaned prior to analysis. Approximately 4 Å of film thickness was removed by the cleaning process. C/Al ratio was quantified by comparing normalized peak areas in C 1s and Al 2p regions. Peak areas were normalized by sensitivity factors.

Figure 3.2 contains AES depth profiles of nominally 125 Å thick films deposited at three substrate temperatures. Surface atoms were removed by an argon ion beam while spectral data was collected simultaneously. Aluminum, oxygen, and carbon signals were observed for sputter times less than approximately 15 minutes. Based on the sputter time required to achieve spectra indicative of the interface region, the film etch rate was calculated to be approximately 10 Å/min. Greater depth resolution was achieved due to the slower etch rate of this process compared to the XPS depth profile presented in Chapter II.
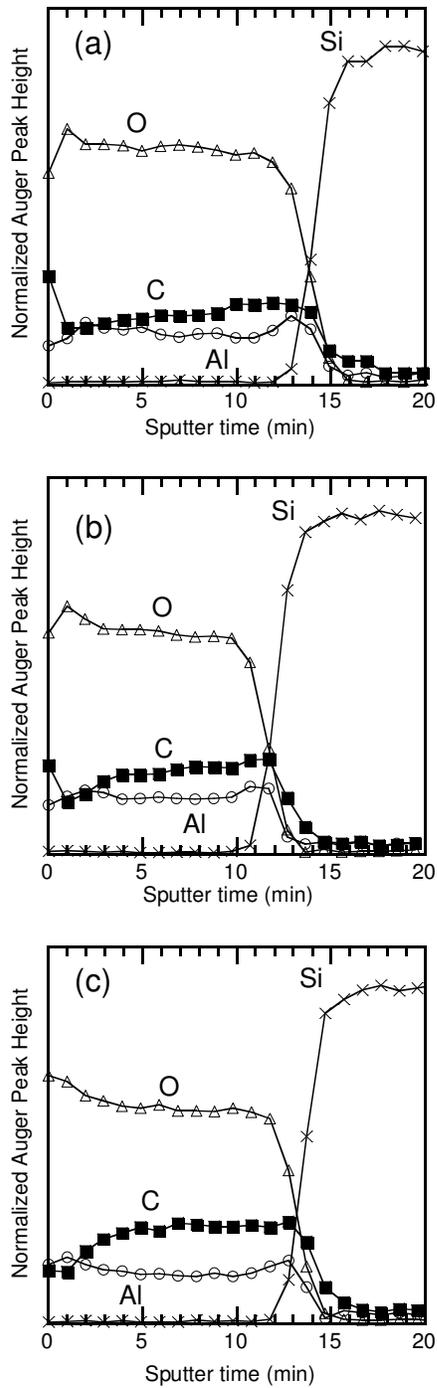
Figure 3.2 - AES depth profiles of nominally 125 Å thick aluminum oxide films deposited at temperatures: (a) 538 °C, (b) 599 °C, (c) 659 °C. Peak-to-peak heights were normalized using published sensitivity factors.

Spectral intensities were quantified using a method similar to the quantification of XPS data presented in Chapter II. The total amount of carbon in the film was estimated by the area under the carbon signal. The area under the curve increased as deposition temperature increased, suggesting that the amount of carbon in the film increased as deposition temperature increased. This observation was in agreement with XPS results presented in the previous chapter. The peak height of carbon increased with increased sputter times, which suggested that there was a concentration gradient in the film.

The C/Al ratio observed in the AES depth profiles ranged from approximately 1 to 2 for films deposited in the 538 – 659 °C temperature range. This ratio was nearly an order of magnitude larger than the ratio determined from XPS analysis of films deposited at the same temperatures. The difference in atomic ratios between the two techniques was attributed to the use of sensitivity factors for quantitative analysis. The use of empirical sensitivity factors is an appropriate method for comparing qualitative spectral trends between samples, but sensitivity factor tables are to be used specifically with a certain type of electron analyzer and detection system in order to produce accurate quantitative results. The ratios calculated from XPS data were assumed to be more accurate than the ratios calculated from AES data because the XPS sensitivity factors were developed for the instrument model that was used in this study.

Bonding environment of carbon

In Figure 2.3, high-resolution XPS spectra of the Al 2p and O 1s regions were presented. We will now focus on the C 1s region. Figure 3.3(a) contains XPS spectra collected from films deposited at various temperatures between 417 and 659 °C. Each

spectrum contains a large peak with a binding energy near 285 eV, as well as a smaller peak near 289 eV. To produce Figure 3.3(a), the binding energy scales were shifted so the peak positions of the large peaks were 284.8 eV. We assumed these peaks were observed due to adventitious carbon species that settled on the sample surface during transport in air to the XPS system. The spectra collected from films deposited at temperatures of 538 °C and higher also contain a peak near 281 eV. Figure 3.3(b) contains the spectrum collected from a film deposited at 659 °C, which shows the three highly-resolved peaks.

The position of the peak in an XPS spectrum provides information about the chemical bonding of the material. Reported C 1s binding energies are given in Table 3.1 as well as the type of bond attributed to each range of binding energies.
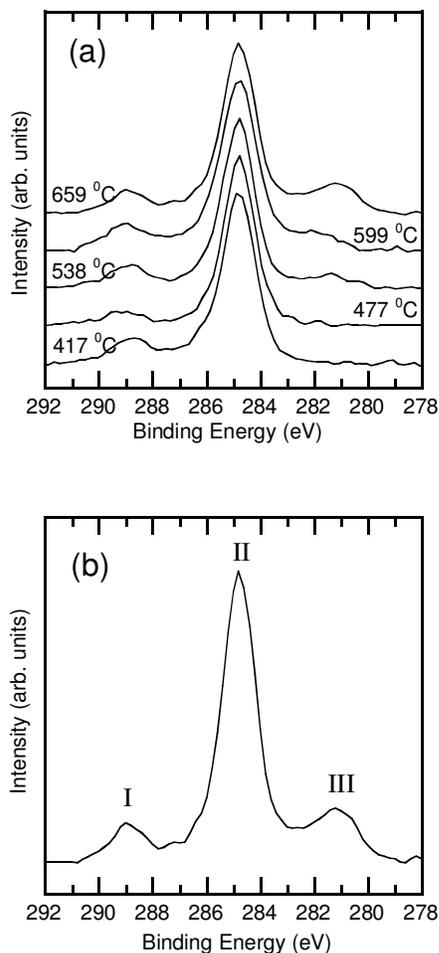
Figure 3.3 - (a) Effect of deposition temperature on XPS peak shape of C 1s region. (b) High-resolution XPS spectrum of C 1s region collected from film deposited at 659 °C. Denoted peaks represent different bonding environments of carbon atoms within film.

Based on the energy ranges given in Table 3.1, the peaks I, II, and III in Figure 3.3(b) were attributed to carbon-oxygen, carbon-carbon, and carbon-metal bonding, respectively. Therefore, carbon-oxygen and carbon-carbon bonding were observed in spectra collected from all films deposited in the 417 – 659 °C temperature range. Carbon-metal bonding was only observed in spectra collected from films deposited at 538 – 659 °C.

Table 3.1. XPS binding energies[†] in C 1s region [2]

Binding energy range (eV)	Compound type
280.8 – 283.0	Carbide (C-metal)
284.3 – 285.1	Carbon (C-H, C-C)
286.1 – 286.7	Alcohol (C-OH)
286.2 – 288.0	Ether (O-C-O)
287.2 – 288.1	Ketone/aldehyde (HC=O)
288.0 – 289.2	Carboxyl (COOH)
289.0 – 291.5	Carbonate (CO_3^{2-})

[†] Binding energy scale calibrated to Au $4f_{7/2}$ = 84.0 eV

Non-destructive depth profiling

Angle-resolved XPS (ARXPS) enables non-destructive depth profiling of the surface region of a sample. Changing the angle between the sample normal and the analyzer via sample tilting changes the takeoff angle of the electrons admitted into the analyzer. Varying the takeoff angle varies the depth into the sample at which electrons can escape and enter the analyzer. Thus, varying the takeoff angle varies the depth of analysis.

The intensity (I) of photoelectrons emitted from a surface is related to the takeoff angle (θ) by a Beer-Lambert relationship given in Equation 3-1. I_0 is the intensity from an infinitely thick, uniform layer at a depth d and λ_{atten} is the attenuation length of a photoelectron traversing through the material. The attenuation length is a function of the kinetic energy of the photoelectron and the properties of the material. Equation 3-1 can be re-arranged to show that the ratio d/λ_{atten} is related to θ (Equation 3-2). For a takeoff angle of 90°, approximately 63% of the observed intensity originates within 1 attenuation

length of the surface, 85% emanates within a depth of $2\lambda_{atten}$, and 95% comes from within $3\lambda_{atten}$ of the surface. However, 95% of the intensity comes from within $1.2\lambda_{atten}$ at a takeoff angle of 30°. Therefore, spectra collected at small takeoff angles are representative of the surface while spectra collected at large takeoff angles provide information from deeper into the material.

$$I = I_0 e^{\frac{-d}{\lambda_{atten} \sin \theta}} \qquad (3\text{-}1)$$

$$\frac{d}{\lambda_{atten}} = \ln\left(\frac{I_0}{I}\right) \sin \theta \qquad (3\text{-}2)$$

Figure 3.4 contains ARXPS spectra of the C 1s region collected from films deposited at 417 and 659 °C. For each plot, spectra were collected at three takeoff angles. The samples were not sputter-cleaned prior to analysis. The heights of the large peaks near 285 eV were normalized, and then the spectra were offset for visual clarity.
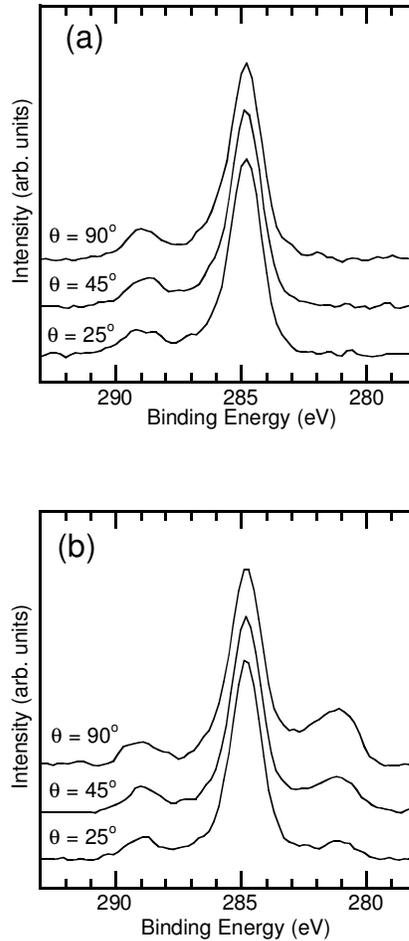
Figure 3.4 - XPS spectra of C 1s region collected from AlO_xC_y films deposited at temperatures: (a) 417 °C, (b) 659 °C. Photoelectron takeoff angle from sample parallel is designated on each spectrum. Larger takeoff angles correspond to deeper information depth.

The spectra shown in Figure 3.4(a) each consisted of a large peak near 285 eV and a smaller peak near 289 eV. The shapes of the peaks and the ratios of the areas between the large and small peaks did not change as a function of takeoff angle. This observation suggests that there is carbon on the surface as well as within the film, and the bonding of the carbon at the surface and in the bulk are similar.

The spectra shown in Figure 3.4(b) consisted of the three resolved peaks described in Figure 3.3(b). The intensity of the peak associated with carbon-metal bonding increased relative to the intensity of the other peaks as takeoff angle increased. The ratio of the area of the peaks associated with carbon-oxygen and carbon-carbon bonding did not change as a function of takeoff angle, similar to the observations discussed in the analysis of Figure 3.4(a). These results suggested that carbon-metal bonding was present in the bulk of the film rather than near the surface.

Correlation of C 1s XPS spectra with Al 2p and O 1s spectra

XPS spectra of the Al 2p and O 1s regions were analyzed to correlate with the observations that the C 1s spectrum changed depending on the deposition temperature. The spectra from the Al 2p and O 1s regions contained single broad peaks, as shown in Figure 2.3, rather than the well-resolved peaks observed in the spectra collected from the C 1s region. Reported Al 2p and O 1s binding energies for compounds in the Al-C-O system are provided in Table 3.2 and Table 3.3, respectively. Note that the binding energy of an Al-C bond is within the reported range of Al-O bonding; likewise, the binding energy of O-C bonding in carbonates is similar to that of the binding energy for O-metal bonds. Deconvolution of the separate binding states was difficult in this case. We used the total peak widths to indicate changes in the peak shape due to contributions from multiple aluminum and oxygen chemical states within the films.

Table 3.2. XPS binding energies[†] in Al 2p region [2]

Binding energy range (eV)	Compound type
72.5 – 73.0	Al metal
73.6 – 74.7	Oxides
73.9 – 74.5	Al_2O_3 (sapphire)
73.6 – 74.3	Al_2O_3 (alpha)
74.0 – 74.6	AlOOH (boehmite)
74.1 [5]	Al-C

[†] Binding energy scale calibrated to Au $4f_{7/2}$ = 84.0 eV

Table 3.3. XPS binding energies[†] in O 1s region [2]

Binding energy range (eV)	Compound type
528.1 – 531.1	Metal oxide (O-metal)
530.9 – 532.0	Hydroxide (O-H)
530.5 – 531.5	Carbonate (CO_3^{2-})
529.9 – 531.8	Al_2O_3

[†] Binding energy scale calibrated to Au $4f_{7/2}$ = 84.0 eV

Figure 3.5 plots Al 2p and O 1s peak widths at the half height above a Shirley background versus deposition temperature. For comparison the Al 2p peak width of a sputter-cleaned aluminum foil was 0.48 eV. Notice that between 477 and 538 °C the width of the O 1s peak steps down from approximately 2.05 eV to 1.86 eV. At deposition temperatures greater than 477 °C the width of the Al 2p peak increases with deposition temperature. The transition coincides with the observation of a carbon-metal peak in the C 1s spectra collected from films deposited at 538 °C and higher.
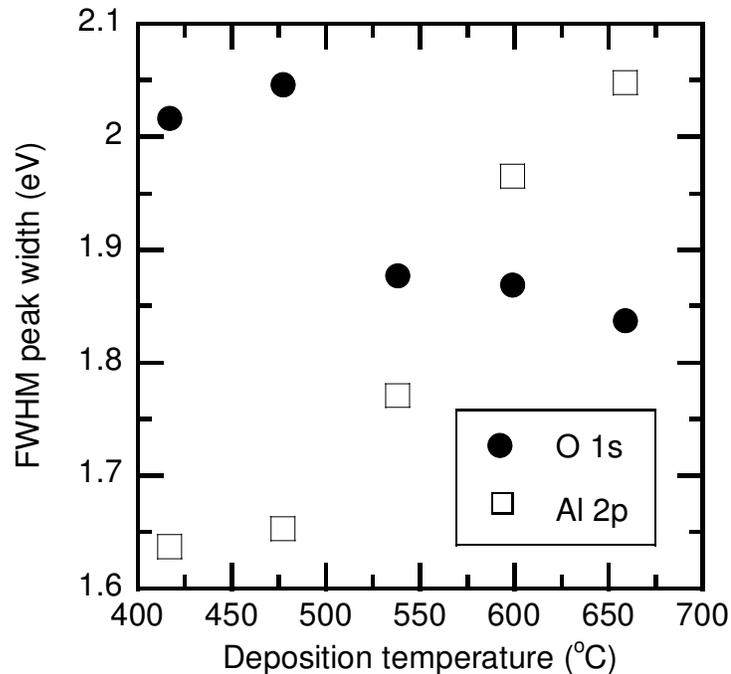
Figure 3.5 – Width of peak in high-resolution XPS spectrum collected from Al 2p and O 1s regions versus deposition temperature. Peak width defined as full width at half-height (FWHM) above Shirley background. Analyzer pass energy was 23.50 eV. Films were deposited via thermal decomposition of dimethylaluminum isopropoxide.

The broadening of the Al 2p peak suggests that aluminum carbide-like species were present in films deposited at temperatures of 538 °C and higher in addition to the oxides species. The data in Figure 3.5 suggests that the increase in the total peak width is due to an increasing contribution of the carbide-like species to the total peak shape. This observation correlated with spectra shown in Figure 3.3(a) which suggested that the concentration of metal carbide species in the film increased with increased deposition temperature.

The width of the O 1s peak changed less with increased deposition temperature than the width of the Al 2p peak for films deposited at 538 °C and higher. The thinning of the O 1s peak suggests that multiple chemical states contribute less to the total peak

width in films deposited at 538 °C and higher than in films deposited at 477 °C and below. This behavior may be attributed to the incorporation of hydroxyl groups into films deposited at 477 °C and below. Hydroxyl group incorporation has been reported for aluminum oxide films deposited through ATI decomposition [6]. In the referenced study, the hydroxyls were lost from the film as water at deposition temperatures above 415 °C.

Flux analysis and comparison to previous studies of DMAI pyrolysis

Results show that aluminum oxide films deposited in this study contained carbon as an impurity. The atomic concentration of carbon in the film was approximately 5% from analysis of XPS spectra. Our observations of film stoichiometry were contrary to the results of Lee [7], who studied DMAI pyrolysis in the 477-727 °C temperature range. In Lee's work the Al:C:O ratio in the films was 1:2:1 and was independent of temperature. In our work, the O/Al ratio was greater than 1, while the C/Al ratio was much lower than 2 and changed with deposition temperature. Koh [8] also reported results from a study of aluminum oxide films produced by DMAI in which carbon-free, stoichiometric films were observed . Our results and Koh's results are interesting in that the deposited films contained O/Al ratios greater than the O/Al ratio in the DMAI molecule. In order to achieve an O/Al ratio in the film greater than one, the deposition process must include steps to either remove aluminum atoms as volatile by-products or introduce extra oxygen atoms. An analysis was performed to determine the contribution of any unexpected oxygen-containing gases that may be present in the reactor during depositions, and whether they could affect the composition of the depositing film.

The base pressure of a vacuum chamber when it is not in use is the pressure where equilibrium is reached between the rate at which gases are pumped out and the rate at which gases enter the chamber by diffusion processes through seals and walls. Background gases are those gases present in the reactor at its base pressure. Flux analysis helped to elucidate the relative rates of processes occurring simultaneously in the reactor. We compared the gas impingement flux ($J_{i,y}$) [Equation 3-3] of both process and background gases to film deposition flux (J_r) [Equation 3-4] where p_y is the partial pressure of gas species y, N_A is Avogadro's constant, R is the universal gas constant, T is the temperature, M_y is the molar mass of y, dh/dt is the linear deposition rate determined by ellipsometry and discussed in Chapter II, ρ_m is the film density, and M_f is the molar mass of the film [9].

$$J_{i,y} = \frac{p_y N_A}{\left(2\pi \, RTM_y\right)^{1/2}} \tag{3-3}$$

$$J_r = \frac{dh}{dt}\left(\frac{\rho_m N_A}{M_f}\right) \tag{3-4}$$

$J_{i,DMAI}$ represents the impingement flux of DMAI molecules and provides a theoretical maximum deposition rate, assuming every precursor molecule that strikes the substrate reacts and decomposes into the growing film. $J_{i,BG}$ represents the impingement flux of a generic background gas species. J_r is calculated from the experimental deposition rate and therefore is more relevant for comparison of actual film deposition and contributions of background gases.

The composition of background gases in our chamber at its base pressure of approximately 10^{-7} Torr was determined using a quadrupole mass spectrometer (Stanford Research Systems RGA300, Sunnyvale, CA, USA). The mass spectrometer was mounted to a port on the side of the reactor at a height near the sample holder assembly, and could be isolated from the chamber by a gate valve during deposition runs. Figure 3.6 contains the mass spectrum of gases present in the reactor prior to a deposition run. The wall and substrate heaters were maintained at 150 and 500 °C, respectively, to simulate conditions during a deposition. Major peaks were observed in the mass spectrum at mass-to-charge (m/z) values of 28, 14, 32, 18, and 44. These were assigned to N_2^+, N^+, O_2^+, H_2O^+, and CO_2^+, respectively, which suggests that oxygen-containing gas species were present in the reactor along with the process gases DMAI and N_2. No peaks were observed at m/z values larger than 44. The partial pressure of each peak was scaled so that the total pressure was equal to the pressure indicated by a pressure gauge located near the mass spectrometer.
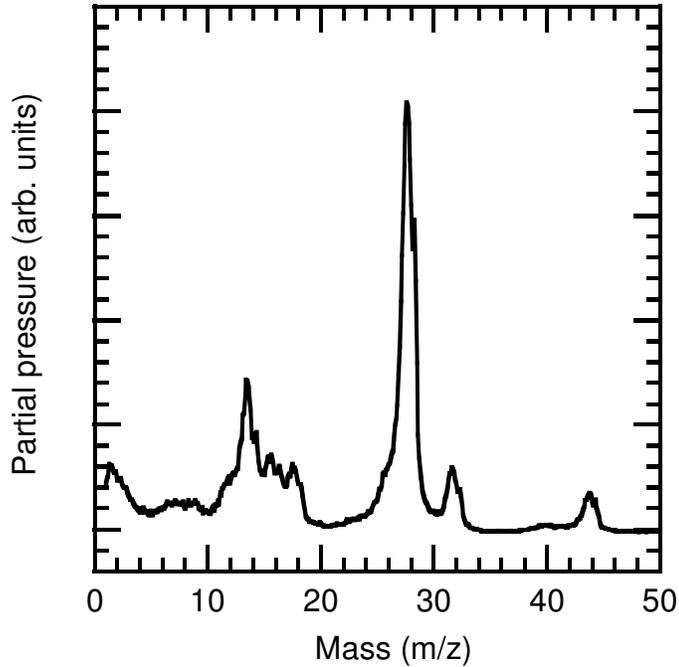
Figure 3.6 - Mass spectrum of background gases in HV-CVD chamber at base pressure. The wall temperature was 150 °C. Substrate heater was set to 500 °C. No process gases were introduced into the chamber during the collection of this spectrum.

The reactor in this work was not assumed to be well-mixed, due to the orientation of the pumping system. Therefore, order-of-magnitude estimations of impingement and deposition fluxes calculated under deposition conditions for this work are provided in Table 3.4. Flux estimations were also calculated from information provided in the Koh and Lee studies and included for comparison. No information is provided in the Koh or Lee studies regarding the composition of background gases, so we assumed that the compositions of background gases in their reactors were similar to the composition of background gases in this work. Variables in Equation 3-3 such as temperature and gas mass were generally within an order of magnitude for each study, suggesting that the actual gas composition is not important as long as oxygen-containing species are present.

The main difference in impingement rate between each of the studies is determined by the value of pressure, which varies by order of magnitudes.

Table 3.4. Comparison of fluxes from background gases and film deposition (all flux values in units of molecules $m^{-2} s^{-1}$)

Flux	Description	$\log_{10}$(flux value)	Reference
$J_{i,DMAI}$	Impingement of DMAI	21.5	This work
$J_{i,BG}$	Impingement of background gas	18	This work
J_r	Film deposition flux	18	This work
$J_{i,O2,Koh}$	Impingement of background gas (Koh)	20.5	[8]
$J_{r,Koh}$	Film deposition flux (Koh)	18	[8]
$J_{i,O2,Lee}$	Impingement of background gas (Lee)	14.5	[7]

As shown in Table 3.4, $J_{i,DMAI}$ exceeds $J_{i,BG}$ by several orders of magnitude. This calculation suggests many more DMAI molecules strike the substrate in a given time than background gas molecules, and therefore the contribution of oxygen-containing background gases in the deposition process would be minimal. However $J_r/J_{i,BG} \sim 1$, meaning that the actual film deposition flux is roughly the same order of magnitude as the impingement rate of background gas species. Thus, it is reasonable to consider that oxygen atoms could be contributed by background gases and participate in the deposition mechanism. The discrepancy between $J_{i,DMAI}$ and J_r suggests that the reactive sticking coefficient of DMAI is on the order of 10^{-3}.

The estimated flux of background gases in Koh's work exceeds the observed deposition flux by approximately 2 orders of magnitude. The abundance of oxygen atoms in background gas species would be sufficient to completely oxidize the aluminum

atom in DMAI while removing carbonaceous ligands. On the other hand, the impingement rate of background gases in Lee's work is much lower than in this work and in Koh's work. Although Lee did not provide deposition rate data, a linear deposition rate of 10^{-4} Å/min would be required to achieve similar orders of magnitude for the impingement and deposition fluxes. Therefore we assume that background gases did not contribute to the films deposited in Lee's work.

<div align="center">Conclusions</div>

The location and chemical bonding of carbon atoms in aluminum oxide films were investigated in this chapter. XPS analysis of the C 1s region suggested that carbon-metal bonds exist within films deposited at temperature of 538 °C and higher. The source of carbon-metal bonding within the film could be incomplete decomposition of the Al-CH$_3$ groups in the precursor. Carbon-oxygen and carbon-carbon bonding were observed in spectra collected from samples deposited at lower temperatures. Each of those types of bonds is found within the DMAI structure. The observation of carbide bonding can be correlated to the availability of oxygen-containing background gases in the reactor during depositions.

An order-of-magnitude flux analysis provided insight into the relative rates of gas impingement and film growth. Deposition rate spanned approximately three orders of magnitude under the process conditions used in this study, as shown in Chapter II. At the middle decade of the deposition rate (around 538 °C as the deposition temperature), the impingement flux of oxygen-containing background gases was approximately the same order of magnitude as the film deposition flux. At higher temperatures and deposition

rates, the deposition flux is greater than the impingement flux, and this results in the incomplete decomposition of precursor bonds. At a deposition temperature of 417 °C, the deposition rate is approximately 0.2 Å/min, and so the impingement rate is greater than the deposition rate by approximately an order of magnitude. Thus, there are sufficient numbers of oxygen atoms in the chamber to break the Al-C bonds in the precursor.

REFERENCES

1. Yablonovitch, E., D.L. Allara, C.C. Chang, T. Gmitter, and T.B. Bright, *Unusually Low Surface-Recombination Velocity on Silicon and Germanium Surfaces.* Physical Review Letters, 1986. **57**(2): p. 249-252.

2. John F. Moulder, W.F.S., Peter E. Sobol, Kenneth D. Bomben, *Handbook of X-ray photoelectron spectroscopy*, ed. R.C.K. Jill Chastain, Jr. 1995, Chanhassen, Minnesota: Physical Electronics USA, Inc.

3. Fairley, N., *CasaXPS*. 2008.

4. Kenton D. Childs, B.A.C., Lori A. LaVanier, John F. Moulder, Dennis F. Paul, William F. Stickle, David G. Watson, *Handbook of Auger electron spectroscopy*. Third ed, ed. C.L. Hedberg. 1995, Eden Prairie: Physical Electronics, Inc.

5. Hinnen, C., D. Imbert, J.M. Siffre, and P. Marcus, *An in-Situ Xps Study of Sputter-Deposited Aluminum Thin-Films on Graphite.* Applied Surface Science, 1994. **78**(3): p. 219-231.

6. Gleizes, A.N., C. Vahlas, M.M. Sovar, D. Samelor, and M.C. Lafont, *CVD-Fabricated aluminum oxide coatings from aluminum tri-iso-propoxide: Correlation between processing conditions and composition.* Chemical Vapor Deposition, 2007. **13**(1): p. 23-29.

7. Lee, S.Y., B. Luo, Y.M. Sun, J.M. White, and Y.S. Kim, *Thermal decomposition of dimethylaluminum isopropoxide on Si(100).* Applied Surface Science, 2004. **222**(1-4): p. 234-242.

8. Koh, W., S.J. Ku, and Y. Kim, *Chemical vapor deposition of Al2O3 films using highly volatile single sources.* Thin Solid Films, 1997. **304**(1-2): p. 222-224.

9. Smith, D.L., *Thin-film deposition : principles and practice*. 1995, New York: McGraw-Hill. xxiii, 616 p.

CHAPTER IV

ELECTRICAL CHARACTERIZATION OF MOCVD
ALUMINUM OXIDE THIN FILMS

Introduction

The International Technology Roadmap for Semiconductors (ITRS) is a set of

goals established by the semiconductor industry related to challenges in the scaling of

microelectronic devices. The 2007 edition of the ITRS [1] dictates that the thickness of

the gate oxide in metal-oxide-semiconductor field-effect transistors (MOSFET) should be

1 nm or less. At such small thicknesses silicon dioxide gate oxides exhibit large leakage

currents due to electron tunneling from the substrate to the gate metal. Leakage current

causes increased power consumption and difficulty maintaining the switching state of the

MOSFET. Aluminum oxide is one of several materials under investigation to replace

SiO_2 as the gate dielectric [2].

In this chapter, the dielectric properties of chemically vapor deposited aluminum

oxycarbide films were investigated. The effect of annealing on electrical properties was

also investigated.

Experimental details

Film deposition

N-type Si (100) substrates with resistivity of 1-10 Ω-cm were used. The substrates were dipped in a 2 vol% HF/ DI water solution for 90 sec to remove the native oxide, then rinsed with DI water for 2 minutes, and blown dry with nitrogen.

Nominally 100 Å thick aluminum oxide films were deposited in a HV-CVD system using dimethylaluminum isopropoxide as the precursor and deposition conditions described in Chapter II. Films were deposited at 599 °C.

Annealing

Annealing is the heating of a material to a temperature below its melting point, and is used in microchip manufacturing after various process steps to reform broken bonds or promote diffusion of dopant atoms. In this study, films were annealed 30 minutes at a temperature of 400 °C. Three types of annealing environments were chosen for investigation. Vacuum anneals were performed in the HV-CVD system used for film deposition. The chamber pressure during annealing was approximately 3×10^{-7} torr. Samples were radiatively heated by a heat source located approximately 1 cm away. N_2 annealing was performed in the HV-CVD chamber using ultrahigh purity nitrogen at a flow rate of 25 sccm and total reactor pressure of 0.5 Torr. A butterfly valve installed between the reaction chamber exit and turbo pump inlet was used to regulate pressure in the chamber by adjusting the gas conductance at the pump inlet. Air anneals were performed in a quartz tube furnace with both ends open to atmosphere. Oxygen

annealing was not performed in the HV-CVD chamber due to compatibility issues with the substrate heater.

Fabrication of MOS capacitors

MOS capacitors were constructed to analyze the electrical properties of the oxide films. Aluminum was evaporated through a shadow mask onto the oxide to form 0.208 mm^2 gate electrodes. The silicon backside was roughened with sandpaper to mechanically remove the native oxide layer, and then aluminum was evaporated onto the roughened surface to form an Ohmic contact. Figure 4.1 is a schematic of the capacitor structure.

300 nm Al		300 nm Al
100 Å AlO$_x$C$_y$ film		
1-10 Ω-cm n-type Si(100)		
150 nm Al		
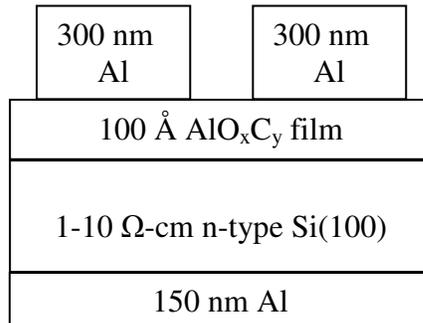
Figure 4.1 - Schematic of Al/AlO$_x$C$_y$/n-type Si(100)/Al capacitor structure for electrical characterization.

Reference capacitors containing a thermal SiO$_2$ dielectric film were also fabricated. The SiO$_2$ layer was grown by an outside vendor. Similar Al/SiO$_2$/Si/Al structures were produced using by the methods described above.

Characterization

Capacitance-voltage (C-V) measurement was performed on a Hewlett-Packard 4284A Precision LCR Meter. A frequency of 1 MHz was applied to the capacitor while the DC voltage was swept from depletion to accumulation in 0.05 V steps. Film composition was determined by X-ray photoelectron spectroscopy. Film thickness was determined by *ex situ* spectroscopic ellipsometry (J. A. Woollam, Inc. M-2000D, Lincoln, NE).

Results and discussion

Metal-oxide-semiconductor theory

The basic structure of a MOSFET was shown in Figure 1.1 and is reproduced here as Figure 4.2. The gate material is separated from the semiconductor substrate by an electrically insulating dielectric layer. The substrate is typically doped to enhance the number and type of electrical charge carriers, and is considered n-type if the majority of carriers are electrons or p-type if the majority of carriers are holes. Carriers in the substrate are either attracted to or repelled from the substrate/dielectric interface depending on the polarity of the gate bias. Under "accumulation," majority carriers are attracted to the interface, and the system acts as a parallel plate capacitor. At a condition known as "inversion", the concentration of minority carriers (e.g., holes in an n-type substrate) at the interface exceeds the concentration of majority carriers, thus creating a conducting channel of charged carriers at the substrate/dielectric interface. Once the

channel is established, current can flow between the source and drain electrodes if a bias

is applied.
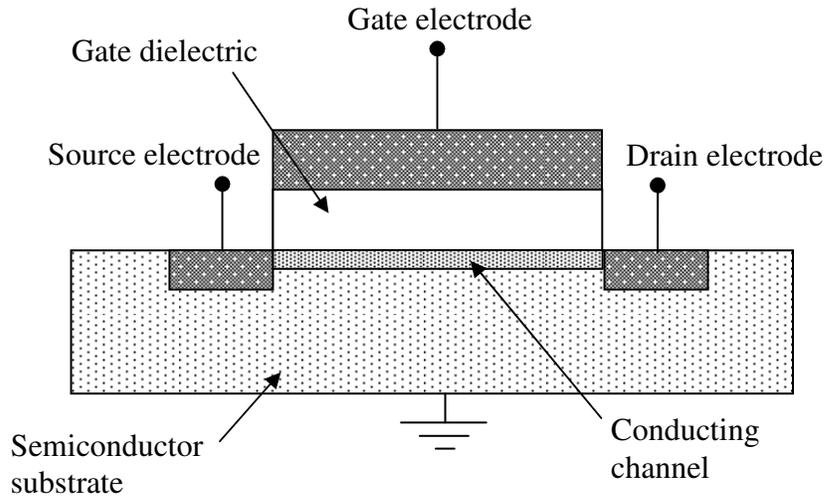
Figure 4.2 - Schematic of MOSFET device

In an ideal MOS capacitor, the gate dielectric does not contain any sources of

charge and there are smooth abrupt interfaces between the dielectric and semiconductor.

A useful reference point is the flat band voltage ($V_{fb,ideal}$). The flat band voltage

corresponds to the difference in work functions between the gate metal (Φ_M) and

semiconductor (Φ_S). The capacitance at the flat band condition (C_{fb}) is given in Equation

4-1, where C_{ox} is the areal capacitance under accumulation conditions, ε_S is the

permittivity of the semiconductor, and L_D is the Debye length, which is defined in

Equation 4-2. In Equation 4-2, k_B is Boltzmann's constant, T is temperature, q is the

charge of an electron, and N_d is the number density of electron donors in the

semiconductor.

$$C_{fb} = \frac{1}{1/C_{ox} + L_D/\varepsilon_S} \tag{4-1}$$

$$L_D = \sqrt{\frac{\varepsilon_S k_B T}{q^2 N_d}} \tag{4-2}$$

In real systems, there are defects within the oxide and at the interface, and they affect the C-V characteristics of the device. There are four main types of charges: interface trapped charge (Q_{it}), interface fixed charge (Q_f), dielectric trapped charge (Q_{ot}), and mobile charge (Q_m). Their general locations are shown in Figure 4.3. Mobile charge carriers such as sodium or potassium ions may be introduced into the dielectric through skin contact, so gloves are typically worn while handling samples. Intrinsic defects of the dielectric material are the source of trapped and interface charges. The interface trapped charge may be caused by dangling bonds at the semiconductor surface.
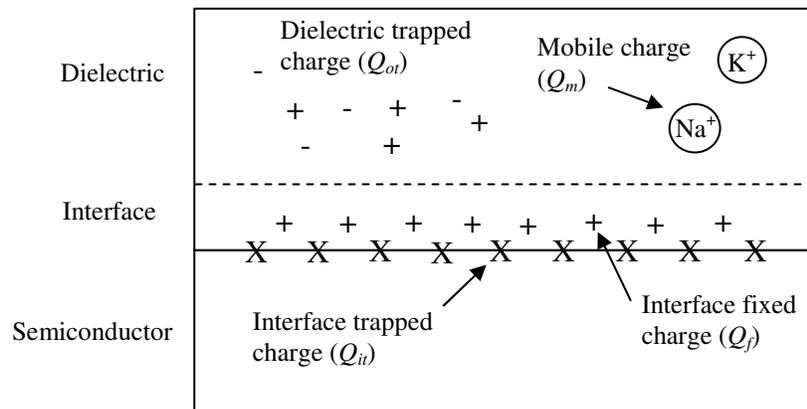
Figure 4.3 - Description of charges found in dielectric/semiconductor region of real MOS devices

The amount of oxide charge can be extracted from the C-V curve based on the shift in flat band voltage (ΔV_{fb}), as shown in Equation 4-3, where Φ is the work function of the gate metal (Φ_M) or semiconductor (Φ_S) and ρ represents some arbitrary profile of electric within the dielectric. The first term that makes up ΔV_{fb} relates to fixed charge at the interface, while the second term includes all charges within the bulk of the dielectric.

$$V_{fb,real} = V_{fb,ideal} + \Delta V_{fb} = (\Phi_M - \Phi_S) - \frac{Q_f}{C_{ox}} - \frac{1}{C_{ox}} \int_0^d \frac{x}{d} \rho(x) dx \qquad (4\text{-}3)$$

Capacitance-voltage characteristics

Figure 4.4 contains capacitance-voltage curves for the four samples investigated in this study. The shape of the as-received (hereafter referred to as sample H1), vacuum-annealed (H2), N_2-annealed (H3), and air-annealed (H4) samples were nearly identical. The capacitance curve of sample H4 exhibited the same shape as the other samples, but was shifted to more negative gate voltages. The relative dielectric constants (ε_r) of the films were extracted from the accumulation regime of the C-V curves using Equation 4-4, where d is the film thickness and ε_0 is the permittivity of vacuum. The accumulation regime was determined where capacitance flattened out at a maximum value as gate voltage was increased. We assumed the value of the capacitance under accumulation conditions was indicative of only the oxide capacitance and did not include any effects of charge carrier depletion in the substrate.

$$\varepsilon_r = \frac{C_{ox}d}{\varepsilon_0} \tag{4-4}$$

A summary of the electrical parameters is given in Table 4.1. The dielectric

constant of the reference SiO_2 film (C-V curve not shown) is also included. The

dielectric constant of each of the alumina films was below the expected value for Al_2O_3

($\varepsilon_r \sim 9$). In addition, the relative dielectric constants of the deposited films were similar

to or below the dielectric constant of SiO_2 ($\varepsilon_r = 3.9$).
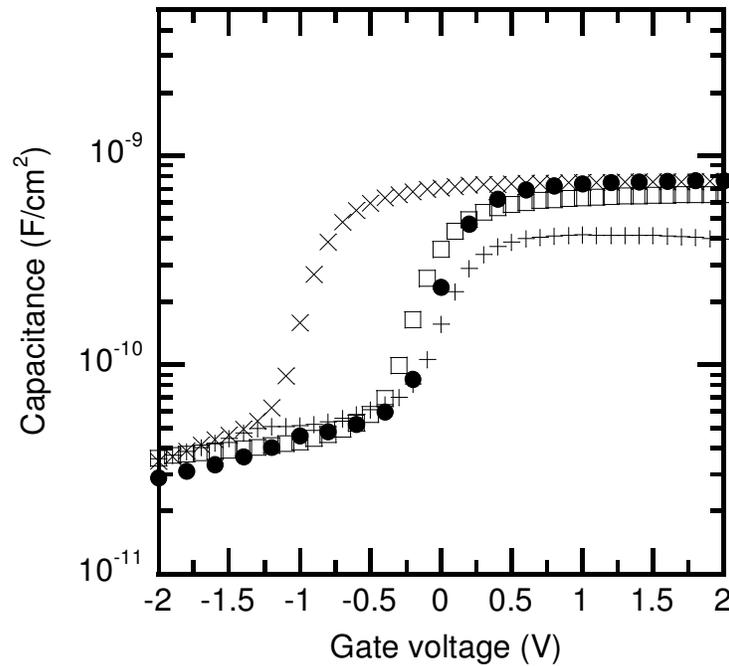
Figure 4.4 – Capacitance-voltage characteristics of Al/AlO$_x$C$_y$/n-type Si(100)/Al
capacitors at 1 MHz bias. Annealing conditions: as-received (square), vacuum anneal
(cross), N$_2$ anneal (circle), air anneal (X).

Table 4.1. Electrical properties of AlO_xC_y dielectric films deposited at 599 °C

Sample ID	Annealing description	Thickness (Å)	C_{ox} (nF/cm^2)	ε_r
H1	None, as-received	106.67	333.0	4.0
H2	Vacuum anneal	104.05	208.0	2.4
H3	N_2 anneal	95.01	384.0	4.1
H4	Air anneal	89.74	379.5	3.8
SiO$_2$ (reference)	-	1381	26.5	4.1

A possible source of error in the calculation of the relative dielectric constants is the use of inaccurate film thicknesses in Equation 4-4. The dielectric constant of the SiO$_2$ film was greater than the expected value of 3.9. Thermal oxides are very reproducible, and this observation suggested the measured film thickness was inaccurate. Assuming the dielectric constant of the thermal SiO$_2$ film is 3.9, the film thickness calculated from Equation 4-4 is 1303 Å, which is 5.6% smaller than the thickness determined from ellipsometry. Therefore, the film thicknesses in Table 4.1 may be overestimates of the true film thicknesses. Based on Equation 4-4, film thickness is directly proportional to ε_r, so the calculated values for the dielectric constants of the films may also be overestimates of the true dielectric constants.

Film density may also explain the lower-than-expected relative dielectric constants of the deposited films. In Chapter II we showed that the refractive index of a deposited film increased and thickness decreased after vacuum annealing at 599 °C, and the changes were attributed to film densification. A lower annealing temperature was used in this chapter, which would tend to decrease the rate of densification during annealing. Air ($\varepsilon_r \sim 1$) has a lower dielectric constant than aluminum oxide. Therefore

the dielectric constant of a low-density aluminum oxide film is expected to be less than the dielectric constant of a fully dense film due to the presence of air within the film.

Another possible explanation for the low dielectric constant is the presence of an aluminum silicate layer (Al-O-Si bonding) at the film/substrate interface with a dielectric constant smaller than that of pure aluminum oxide [3]. The reciprocal of the total capacitance (C_{total}) is related to the reciprocal capacitance of each layer in series, as shown in Equation 4-5, where C_{oxide} is the capacitance of the desired dielectric material and $C_{silicate}$ is the capacitance of the undesirable silicate layer.

$$\frac{1}{C_{total}} = \frac{1}{C_{oxide}} + \frac{1}{C_{silicate}} \tag{4-5}$$

Figure 4.5 contains the C-V plots shown in Figure 4.4 after normalization to the oxide capacitance under accumulation. As mentioned above, the shapes of the plots for each sample are nearly the same. From Equation 4-4, $V_{fb,ideal}$ in this work is -0.8 V based on the work functions of the aluminum gate metal ($\Phi_M = 4.1$) and silicon substrate ($\Phi_S = 4.9$) [4]. The C-V plot of the sample H1 was shifted towards positive gate voltages ($\Delta V_{fb} > 0$). This shift suggested that there were negative fixed charges within the oxide. Aluminum oxide films often contain negative fixed charge, while other dielectrics such as HfO_2 and ZrO_2 tend to contain positive fixed charges [2]. ΔV_{fb} of samples H2 or H3 was approximately the same as sample H1. The data from sample H4 is shifted approximately 0.8 V towards negative voltages from the data displayed for samples H1, H2, and H3. ΔV_{fb} of sample H4 is approximately zero, and suggests that fixed charge in the oxide was reduced due to the air annealing process.
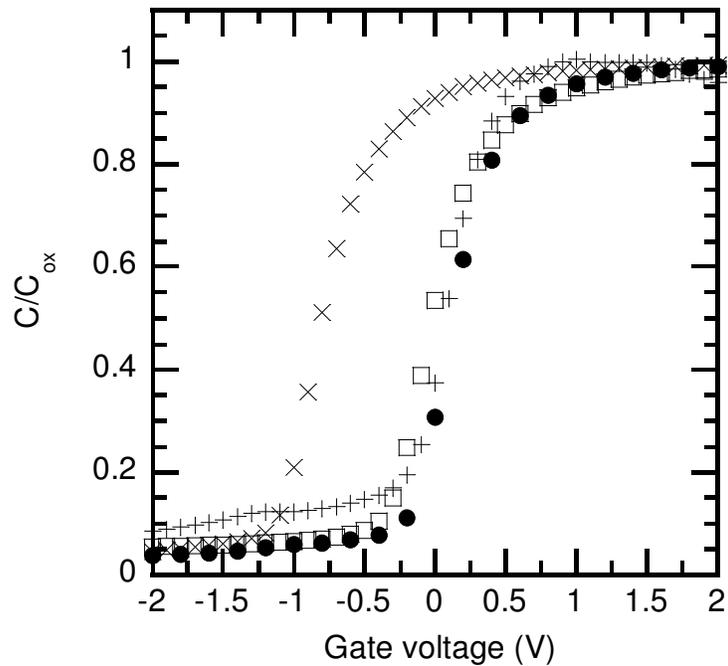
Figure 4.5 - Capacitance-voltage characteristics of Al/AlO$_x$C$_y$/n-type Si(100)/Al capacitors at 1 MHz bias, normalized to C$_{ox}$. Annealing conditions: ss-received (square), vacuum anneal (cross), N$_2$ anneal (circle), air anneal (X).

Material characterization

Annealed samples were analyzed by XPS to correlate electrical behavior to material changes. High-resolution spectra were collected from the Al 2p, O 1s, and C 1s regions of each sample. Table 4.2 compares the ratios of regional peak areas of spectra collected from each sample to those of the sample H1, which was not annealed. Sample H4 had nearly identical peak areas to the peaks observed in the spectrum from H1. The areas of the peaks from H2 were all greater than the areas from H1, but the ratio was nearly the same for each region. This suggests that there was an overall higher signal intensity for the sample H2, rather than actual changes in composition. Sample H3 had a relatively large increase in the area of the carbon peak relative to the areas of the

aluminum or oxygen peaks. We also noted a small peak indicative of fluorine in the

survey spectrum collected from H3, which was assumed to originate from the CVD

chamber used for annealing. Based on Table 4.2, there does not appear to be a

correlation between electrical behavior and film composition.

Table 4.2 XPS peak areas after background subtraction, relative to
background-subtracted peak area of as-received sample

Annealing description	Al 2p	O 1s	C 1s
As-received (H1)	1	1	1
Vacuum (H2)	1.19	1.08	1.19
N_2 (H3)	1.06	0.98	1.26
Air (H4)	1.00	1.02	0.99

Figure 4.6 contains high resolution XPS spectra collected from the C 1s region. The spectra collected from sample H1 exhibited three well-resolved peaks. In Chapter III, these peaks were attributed to C-O, C-C, and C-metal bonding. There was no carbon-metal peak in the spectrum collected from sample H4, which suggests that the bonding configuration of carbon atoms within the film changed during the air anneal. As noted above, XPS results suggest the overall stoichiometry of the film did not change due to the annealing treatments.
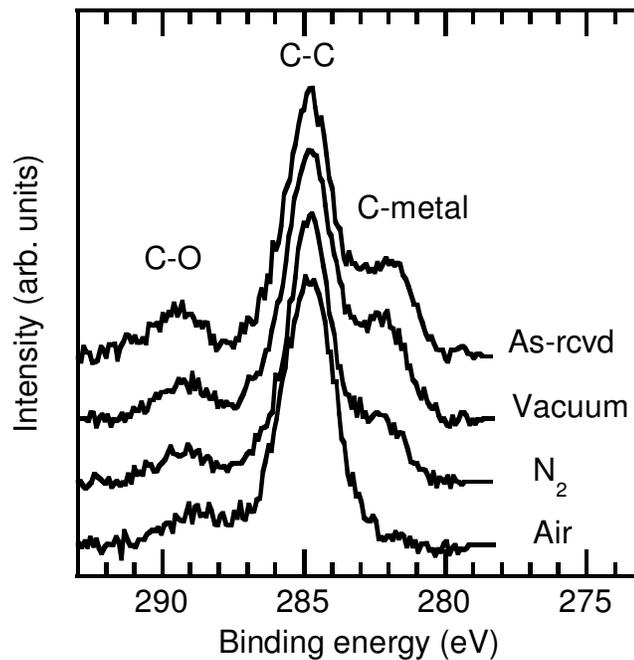
Figure 4.6 - XPS spectra of C 1s region after annealing treatments. Spectral peak positions were calibrated at 284.8 eV, and background intensity was removed by using Shirley background model. Spectra are offset for visual clarity.

Conclusions

In this chapter, electrical properties of aluminum oxycarbide thin films were evaluated by C-V analysis. The effect of annealing in multiple environments was also

discussed. The relative dielectric constant of each of the deposited films was below the expected value for aluminum oxide. The dielectric constant of the film slightly changed after annealing under vacuum, nitrogen, or air at 400 °C for 20 minutes, but did not approach the expected value of approximately 9. Aluminum silicate formation at the film/substrate interface may explain the low dielectric constants and is explored in Chapter IV. The film that was annealed in air exhibited a shift in the flat band voltage that suggested the removal of fixed charge within the film. The absence of XPS peaks representative of carbon-metal bonding in the air-annealed sample suggests that fixed charge in the dielectric film is correlated to the presence of aluminum-carbon bonding within the film.

Materials under investigation to replace SiO_2 as the gate dielectric must exhibit a dielectric constant greater than that of silica so that a layer physically thicker than SiO_2 layer can provide the same capacitance, in accordance with Equation 4-4. The dielectric constants of the films in this study were comparable to those of silica, and therefore did not exhibit favorable characteristics for this application.

REFERENCES

1.	*Front End Processes*, in *The International Technology Roadmap for Semiconductors*. 2007, International SEMATECH: Austin, Texas.

2.	Wilk, G.D., R.M. Wallace, and J.M. Anthony, *High-kappa gate dielectrics: Current status and materials properties considerations.* Journal of Applied Physics, 2001. **89**(10): p. 5243-5275.

3.	Klein, T.M., D. Niu, W.S. Epling, W. Li, D.M. Maher, C.C. Hobbs, R.I. Hegde, I.J.R. Baumvol, and G.N. Parsons, *Evidence of aluminum silicate formation during chemical vapor deposition of amorphous Al2O3 thin films on Si(100).* Applied Physics Letters, 1999. **75**(25): p. 4001-4003.

4.	Muller, R.S., T.I. Kamins, and M. Chan, *Device Electronics for Integrated Circuits*. 3 ed. 2003, New York: John Wiley & Sons.

CHAPTER V

INITIAL STAGE DEPOSITION OF MOCVD ALUMINUM OXIDE THIN
FILMS ON HYDROGEN-TERMINATED SILICON (100)
AND SILICON (100) NATIVE OXIDE SUBSTRATES

Introduction

Coating processes are often used in order to establish a property at the surface that is not found in the bulk of a material. The efficacy and lifetime of the coating depends in part on the interaction between the coating and the substrate. Analysis of chemical bonding states in the interfacial region between the film and the substrate can provide insight into the relative strength of the adhesion between materials.

In this chapter, the early stages of the depositions of aluminum oxide onto silicon substrates are investigated. We used *in situ* spectroscopic ellipsometry to monitor the deposition process within the reaction chamber. The interaction of the precursor gas with a hydrophobic H-terminated Si (100) is compared with a hydrophilic OH-terminated silicon native oxide surface.

Experimental details

Hydrogen-terminated Si (100) substrates (H-Si) were prepared by dipping the wafers into a 2 vol% HF/DI water solution for 90 sec, rinsing with DI water for 2 minutes, and blowing dry with nitrogen. Si (100) substrates with a native oxide layer (NO-Si) were removed from their container and loaded into the deposition system without treatment.

MOCVD films were deposited in a HV-CVD system using deposition conditions described in Chapter II. In summary, films were produced via thermal decomposition of dimethylaluminum isopropoxide (DMAI) precursor.

Elemental depth profiling was achieved using a cylindrical mirror analyzer-based, fixed beam Auger electron spectroscopy (AES) system. A 2 keV primary electron beam (45 µA/cm^2 into an unbiased Faraday cup) incident at 10° off sample normal was used. A 1 keV Ar$^+$ ion beam incident at 65° off sample normal was used for depth profiling (8 µA/cm^2). AES data were analyzed using the CasaXPS software [1]. Peak-to-peak heights of the Al *LMM* (70 eV), Si *LMM* (90 eV), C *KLL* (278 eV) and O *KLL* (510 eV) peaks were collected and normalized using sensitivity factors provided by Physical Electronics [2]. Since sensitivity factors for 1 keV primary electrons are not published, the sensitivity factors for 3 keV primary electrons were used.

Deposition dynamics were studied using *in situ* spectroscopic ellipsometry. Ellipsometry optics (J. A. Woollam, M-2000D, Lincoln, NE, USA) were mounted to the HV-CVD chamber behind fused quartz windows and pointed at the center of the substrate. The angle of incidence was nominally 73° off sample normal. During the deposition process psi and delta data were reported every 5 seconds in the photon energy range of 1.25 – 6.46 eV. Data collection was performed in "high accuracy" mode, in which values of psi and delta were collected twice in each reporting interval and averaged. Ellipsometry data were analyzed with EASE software [3].

Elemental identification and chemical bonding states were determined through X-ray photoelectron spectroscopy (Ulvac-PHI Versaprobe XPS Microprobe, Chanhassen, MN, USA). A 25 W monochromatic Al K$_\alpha$ x-ray source was used. The x-ray beam

diameter was 100 μm. Photoelectrons emitted from the sample at 45° takeoff angle were

collected into a spherical capacitor analyzer operating in constant pass energy mode. The

pass energies of survey and high-resolution scans were 187.50 eV and 23.50 eV,

respectively. Surface charge compensation was achieved with a neutralization system

comprised of low energy electrons and Ar^+ ions. XPS data were analyzed using

CasaXPS software [1]. The binding energy scale was calibrated to the Si $2p_{3/2}$ peak of

elemental silicon at 99.3 eV.

Results and discussion

AES depth profiles of 50 Å thick films deposited on H-Si

Figure 5.1 contains AES depth profiles of films deposited at substrate

temperatures of 417 and 659 °C. There is no silicon signal at short sputter times,

suggesting that the films were continuous. The area under the curve of the carbon signal

is larger for the film deposited at 659 °C than the area under the curve for the film

deposited at 417 °C. This observation is consistent with previous conclusions that films

deposited at higher temperatures contained greater concentrations of carbon within the

film. The shape of the carbon signal was similar in the depth profile at each deposition

temperature. The intensity of the carbon signal decreased upon initial sputtering,

increased in the interface regime, and then decreased to zero when the substrate was

reached.
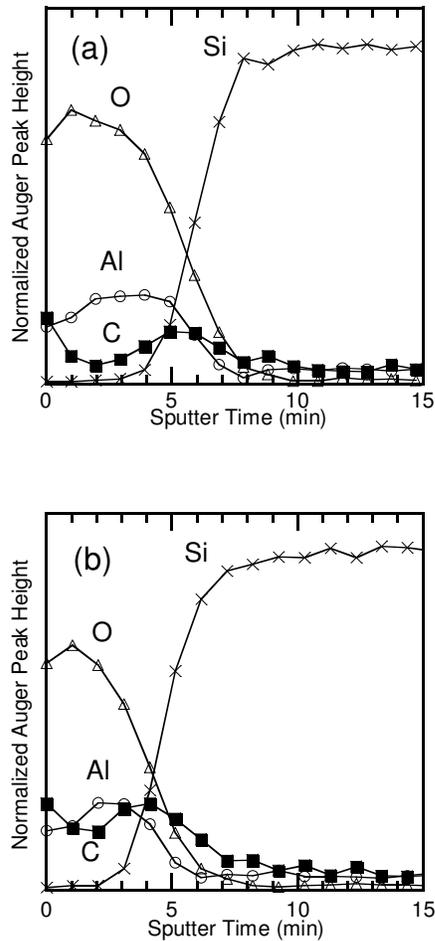
Figure 5.1 - AES depth profiles of nominal 50 Å thick aluminum oxide films. Films were deposited on H-Si via thermal decomposition of dimethylaluminum isopropoxide precursor at substrate temperature: (a) 417 °C, (b) 659 °C

In situ ellipsometry on H-Si and NO-Si

In situ ellipsometry allows one to monitor the dynamics of the deposition process in contrast to *ex situ* ellipsometry where the spectrum reflects one snapshot of the sample. A quasi-dynamic analysis of a deposition process can be achieved through systematic *ex situ* analysis of samples processed for different lengths of time. However, the spectra may not accurately depict the nature of the as-deposited film after removal from the vacuum system due to reactions with ambient gases or the presence of overlayers.

91

In this study, psi and delta data were collected throughout the duration of the deposition, and the film thickness was calculated at each time slice. The film thickness was determined by fitting the psi and delta data to an optical model. The optical model consisted of a single film on a substrate. A "virtual substrate" layer was used to model the optical constants of the substrate. Prior to the deposition, psi and delta data were collected from the bare substrate for approximately 5 minutes. The optical constants of the "virtual substrate" layer were determined from those data using a similar technique as was given in Chapter II for the determination of the optical constants of the substrate by *ex situ* ellipsometry. A Cauchy model was used to describe the optical constants of the film. The Cauchy parameters were chosen to be A = 1.625 and B = 0.01 μm^2 in accordance with the discussion presented in Chapter II regarding the difficulty of fitting both film thickness and optical constants for sub-100 Å thick films. The optical model was fitted to data in the 550 – 995 nm spectral range using film thickness as the only fitting parameter. Figure 5.2 contains a plot of film thickness versus deposition time for a film deposited at 538 °C on a NO-Si substrate.
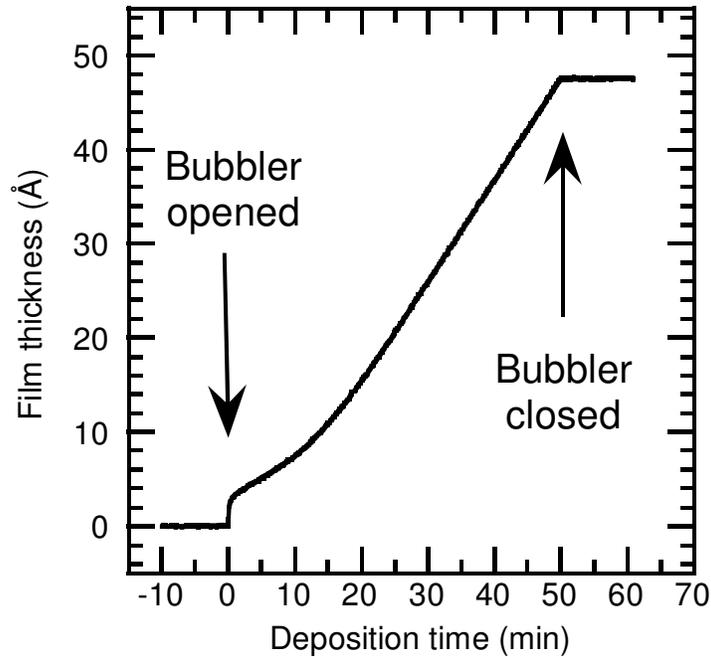
Figure 5.2 – Film thickness evaluated as a function of deposition time. Substrate temperature was 538 °C. Film was deposited on NO-Si substrate. Thickness was calculated by *in situ* ellipsometry every 5 seconds.

The bubbler was opened at the deposition time designated as 0 minutes. The thickness increased immediately upon opening of the bubbler which suggested there was no incubation time for the deposition reaction. The deposition occurred in two regimes: a transient regime from 0 to approximately 20 minutes, and a steady state regime beginning at 20 minutes. The bubbler was closed after approximately 50 minutes of deposition time. The thickness remained constant after the bubbler was closed.

Figure 5.3 compares thickness vs. time plots for samples deposited at 538 °C on different substrate surfaces. The thickness of the film deposited on the H-Si surface increased as soon as the bubbler was open, suggesting there was no incubation period. The onset of deposition was different for the two surfaces. The thickness of the film

deposited on the NO-Si surface jumped to approximately 3 Å immediately when the bubbler was opened. The deposition rate (determined from the slope of the film thickness per time) then decreased for approximately 10 minutes, then increased until a steady state was reached after 20 minutes. On the other hand, there was no jump in the thickness of the film deposited on H-Si when the bubbler opened. The deposition rate reached steady state within approximately 5 minutes. The slopes of the curves in the steady state regime are similar, suggesting that the deposition mechanism in the steady state is independent of the starting surface.
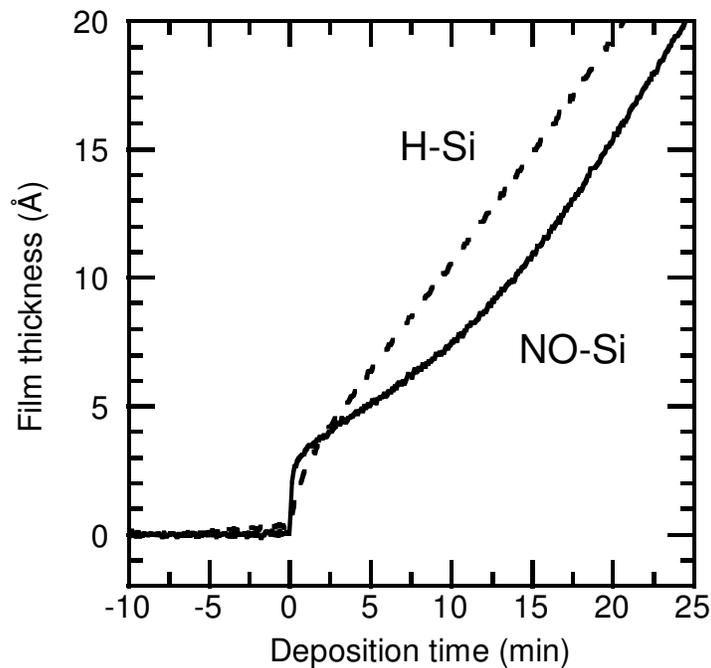
Figure 5.3 – Film thickness during initial deposition onto hydrogen-terminated silicon (100) (H-Si) or Si (100) native oxide (NO-Si). Films were deposited at 538 °C. Film thickness was determined by *in situ* ellipsometry every 5 seconds.

The observed jump in thickness upon bubbler opening for the NO-Si substrate

suggests the rapid formation of a monolayer. An [4] reported that the methyl groups of

the DMAI precursor, which are attached to the aluminum atom, readily react with

hydroxyl groups to produce O-Al bonds and release of CH_4. The NO-Si surface contains

hydroxyl groups, whereas the H-Si surface does not. Slow reaction rates on H-Si

terminated substrates have been reported for several precursors of dielectric films [5].

Characterization of deposition substrates

XPS analysis was used to determine the chemical makeup of the different

substrates. Figure 5.4 contains survey spectra of H-Si and NO-Si substrates. There was

no peak in the H-Si spectra that corresponded to fluorine, which showed that the HF used

to etch the native oxide was completely rinsed away. Peaks corresponding to oxygen and

carbon were observed in the H-Si spectrum.
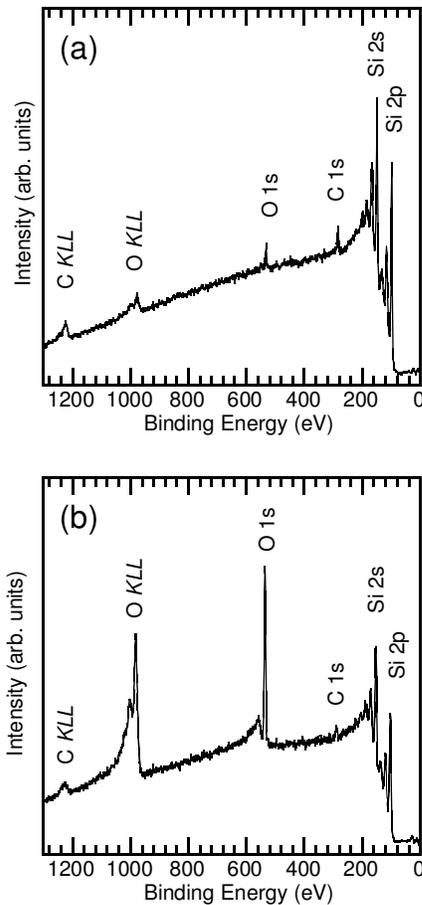
Figure 5.4 - XPS survey spectra of deposition substrates used in the HV-CVD of aluminum oxide thin films: (a) H-Si, (b) NO-Si. Spectra were collected at 90° photoelectron takeoff angle.

Figure 5.5 compares XPS spectra collected from the Si 2p region of each surface type, both before (dotted lines) and after deposition (solid lines). The photoelectron takeoff angle was 30°. Prior to deposition, the spectrum from the H-Si surface contained one doublet peak indicative of the elemental silicon substrate. There was no indication of silicon bonded to oxygen or carbon. Therefore, the carbon and oxygen observed in the survey scan are likely physisorbed to the H-Si surface rather than chemisorbed. The peak near 103 eV binding energy in the NO-Si spectrum was attributed to silicon atoms bound to oxygen in the native oxide layer. After the deposition, there was indication of a peak

around 102 eV binding energy, suggesting the formation of silicate bonding (Si-O-Al) [4]

on both substrates.
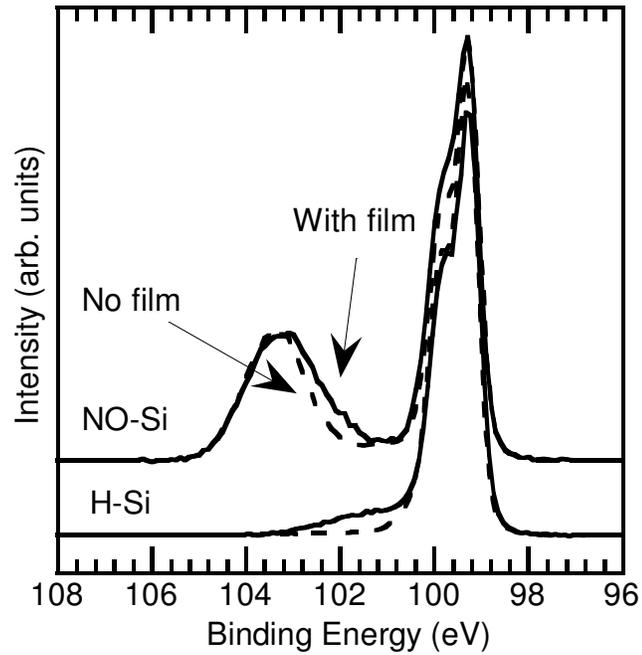
Figure 5.5 - High resolution XPS spectra of Si 2p region before (dotted) and after (solid) 45 second deposition. Substrate temperature was 599 °C. Spectra were collected at 30° photoelectron takeoff angle.
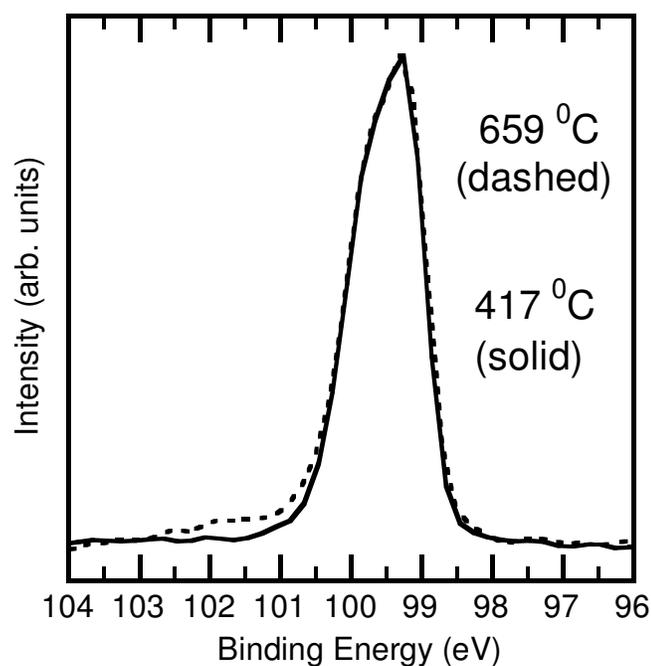
Figure 5.6 - Background-subtracted XPS spectra of Si 2p region for films deposited at 417 °C and 659 °C on H-Si. Spectra were calibrated by setting Si-Si bonding peak position to 99.3 eV. Si-Si bonding peak heights were normalized for better visual comparison of shoulder.

We investigated the Si 2p region using a 90° takeoff angle to determine the effect of deposition temperature on film/substrate interactions of nominally 50 Å thick films. Figure 5.6 shows Si 2p spectra obtained from films deposited at 417 °C and 659 °C on H-Si. The large asymmetric peak at 99.3 eV indicates Si-Si bonds from the substrate [6]. No other peaks are present in the Si 2p region in the spectrum acquired from the film deposited at 417 °C. However, a small peak is observed approximately 2.5 eV to the higher binding energy side in the spectrum from the film deposited at 659 °C. Silicon bonded to aluminum would have a binding energy similar to silicon-silicon bonding, while Si 2p binding energies in SiC and SiO_2 are observed 1.5 [7] and 4 eV [6] to higher binding energies from elemental silicon. Aluminum silicates have reported binding

energies between 2.2 and 3.5 eV above silicon-silicon binding energies [8]. The data in Figure 8 suggests that a silicate is formed during deposition at 659 °C.

Ghosh and colleagues [9] modeled adsorption reaction energetics of a single DMAI molecule interacting with an H-terminated Si (100) surface using surface integrated molecular orbital molecular mechanics, a hybrid quantum mechanics/molecular mechanics method. Ghosh proposed five likely surface reactions, listed below, where an asterisk denotes the surface species:

Methane loss: $Si\text{-}H^* + DMAI \rightarrow Si\text{-}Al(CH_3)\text{-}O\text{-}CH(CH_3)_2^* + CH_4$ (1)
Propane loss: $Si\text{-}H^* + DMAI \rightarrow Si\text{-}O\text{-}Al(CH_3)_2^* + CH_3CH_2CH_3$ (2)
Si methylation: $Si\text{-}H^* + DMAI \rightarrow Si\text{-}CH_3^* + H\text{-}Al(CH_3)\text{-}O\text{-}CH(CH_3)_2$ (3)
Hydrogen loss: $Si\text{-}H^* + DMAI \rightarrow Si\text{-}CH_2Al(CH_3)\text{-}O\text{-}CH\text{-}(CH_3)_2^* + H_2$ (4)
Ring closing: $Si\text{-}Al(CH_3)\text{-}O\text{-}CH(CH_3)_2^* + Si\text{-}H^* \rightarrow Si\text{-}Al(CH_3)^*\text{-}Si + CH(CH_3)_2OH$ (5)
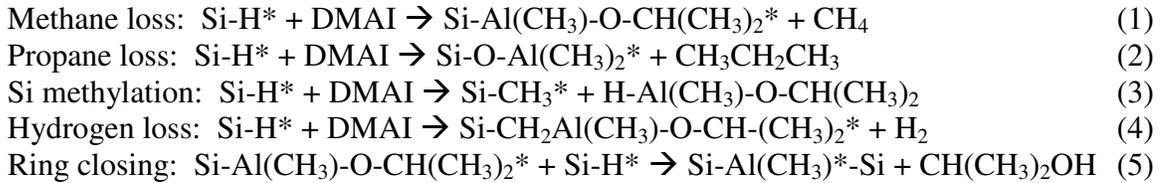
Reactions (1) and (2) are the most thermodynamically favorable, while reaction (1) has the lowest activation energy of 100.5 kJ/mol, approximately 80 kJ/mol lower than reactions (2) and (5). Data in Figure 5.6 shows a lack of Si-C bonding, which supports Ghosh's conclusions that surface reactions creating Si-C bonds are not as favorable as those creating Si-Al or Si-O bonds. Our observation of aluminum silicate-like bonding for films deposited at increased temperature agrees with the mechanism in reaction (2). The propane loss reaction is the most thermodynamically favorable of the five reactions investigated, but has a higher energy barrier than reaction (1). The increase in deposition temperature can supply energy allowing reaction (2) to occur at the surface.

Conclusions

In this chapter, early stages of aluminum oxide deposition on hydrogen-terminated and hydroxyl-terminated silicon (100) substrates were observed. The

deposition rate was faster at the onset of deposition on the OH-terminated surface than the H-terminated surface. Once the films reached approximately 15 Å thick, the deposition rates reached steady state and had similar magnitudes regardless of substrate type. XPS analysis of chemical bonding at the film/substrate interface suggests that methane loss and propane loss are the likely surface reactions, resulting in Si-Al and Si-O-Al bonds. Auger depth profiling suggested that there was carbon at the interface, but it was likely due to carbon overlayers on the substrates prior to the deposition process.

REFERENCES

1.   Fairley, N., *CasaXPS*. 2008.

2.   Kenton D. Childs, B.A.C., Lori A. LaVanier, John F. Moulder, Dennis F. Paul, William F. Stickle, David G. Watson, *Handbook of Auger electron spectroscopy*. Third ed, ed. C.L. Hedberg. 1995, Eden Prairie: Physical Electronics, Inc.

3.   Hale, J. and B. Johs, *EASE*. 2000, J. A. Woollam Co.: Lincoln, NE.

4.   An, K.S., W.T. Cho, K.H. Sung, S.S. Lee, and Y. Kim, *Preparation of Al2O3 thin films by atomic layer deposition using dimethylaluminum isopropoxide and water and their reaction mechanisms.* Bulletin of the Korean Chemical Society, 2003. **24**(11): p. 1659-1663.

5.   Wallace, R.M. and G. Wilk, *Alternative gate dielectrics for microelectronics.* Mrs Bulletin, 2002. **27**(3): p. 186-187.

6.   John F. Moulder, W.F.S., Peter E. Sobol, Kenneth D. Bomben, *Handbook of X-ray photoelectron spectroscopy*, ed. R.C.K. Jill Chastain, Jr. 1995, Chanhassen, Minnesota: Physical Electronics USA, Inc.

7.   Maruyama, B. and F.S. Ohuchi, *H2o Catalysis of Aluminum Carbide Formation in the Aluminum-Silicon Carbide System.* Journal of Materials Research, 1991. **6**(6): p. 1131-1134.

8.   Wagner, C.D., D.E. Passoja, H.F. Hillery, T.G. Kinisky, H.A. Six, W.T. Jansen, and J.A. Taylor, *Auger and Photoelectron Line Energy Relationships in Aluminum-Oxygen and Silicon-Oxygen Compounds.* Journal of Vacuum Science & Technology, 1982. **21**(4): p. 933-944.

9.   Ghosh, M.K. and C.H. Choi, *Adsorption reactions of dimethylaluminum isopropoxide and water on the H/Si(100)-2 x 1 surface: Initial reactions for atomic layer deposition of Al2O3.* Journal of Physical Chemistry B, 2006. **110**(23): p. 11277-11283.

CHAPTER VI

HAFNIUM OXYCARBIDE FILMS PRODUCED FROM
HAFNOCENE PRECURSORS

Introduction

Materials in the Hf-O-C system have shown good stability in the ultrahigh

temperature regime above 1600 °C [1]. Hafnium carbide has a melting temperature of

3928 °C, which is the second highest to tantalum carbide among binary compounds [2].

Hafnium oxycarbide is interesting as an oxidation barrier layer.

We are investigating low temperature synthesis methods to produce coatings of

hafnium carbide and oxycarbide films. There are several advantages to working at lower

temperatures, such as reduced energy costs and safety issues. Also, temperature-sensitive

materials such as organics may be used as substrates. Lastly, thermal mismatch can

cause cracking between films and substrates as samples cool after a high-temperature

deposition process.

Preliminary studies of hafnium-based compounds for use as metal-organic

chemical vapor deposition precursors are presented in this chapter. We are interested in a

liquid precursor that is composed only of the elements needed in our films to reduce the

need for co-reactants or other contaminants. The compounds under investigation are

described in Table 6.1. Each compound is a derivative of hafnocene dichloride, which

consists of two cyclopentadienyl (Cp) groups bound to the metal center, in addition to

two chlorine atoms bonded to hafnium. Alkyl ligands such as methyl groups (Me) or n-

butyl groups (^{n}Bu) were attached either to the Cp group or the hafnium atom. Films were

also produced by a technique of drop casting the precursor from solution. The dropcast

films were analyzed to understand how air exposure affects the precursor compounds.

Table 6.1. Description of hafnocene compounds investigated as CVD precursors in current work

Name	bis(Cp)HfMe$_2$	bis(MeCp)HfMe$_2$	bis(Cp)Hf^{n}Bu$_2$
Structure			
Formula	HfC$_{12}$H$_{16}$	HfC$_{14}$H$_{20}$	HfC$_{18}$H$_{28}$
Molecular weight	338.75	366.80	422.90
T$_{melt}$ (°C)	118 [3]	60 [4]	32-33 [5]
Vapor pressure (mmHg)	sublimes at 0.1 @ 90 °C [6]	0.2 @ 80 °C [7]	--
T$_{decomposition}$ (°C)	450 [8]	450 [9]	< 60 [10]
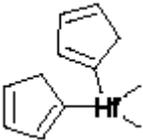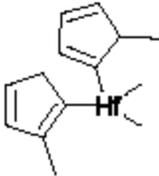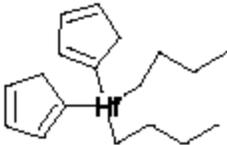
Thermal stability and decomposition mechanisms of metallocene compounds

Chang and Brubaker detected n-alkanes, alkenes, and traces of methane and

ethylene when bis(Cp)Hf^{n}Bu$_2$ was heated to 60 °C in toluene [10]. This observation was

consistent with decomposition through β-hydride elimination. N-butyl metallocenes

decompose through interactions between the metal center and a hydrogen atom bonded to

a β-carbon. 1-butene is eliminated in the reaction as shown in Figure 6.1. Analogous n-

butyl titanocenes and zircocenes decompose around -55 [11] and -40 °C [5], respectively.

The elimination reaction can be suppressed by using shorter alkyl ligands which do not

have β-hydrogens, such as methyl groups, or bulky ligands such as tert-butyl groups

which provide steric hindrances between the metal center and hydrogen atoms.
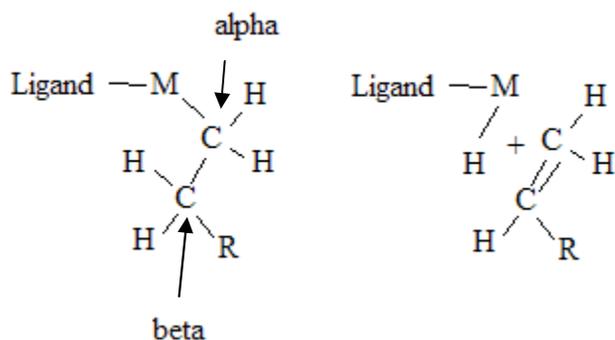
Figure 6.1 - Mechanism of β-hydride elimination in a metal-organic compound

The dimethyl hafnocenes are more stable than di-n-butyl hafnocene. Literature

reports of thermogravimetric analysis of bis(Cp)HfMe$_2$ [12] and bis(MeCp)HfMe$_2$ [13]

showed that each compound evaporated without decomposition at temperatures less than

350 °C. In addition, bis(MeCp)HfMe$_2$ was held at a temperature of 200 °C for 50 hours,

and ^{1}H nuclear magnetic resonance (NMR) spectra did not reveal any indication of

decomposition [13].

Lang and Seyferth [14] studied the pyrolytic decomposition of the zircocene

bis(Cp)ZrMe$_2$ at 1450 °C. ZrC, CH$_4$, HCp, C$_3$H$_4$, and amorphous carbon were reported

as decomposition products. The authors suggested that hydrogen was abstracted from the

Cp ligand to form methane as a decomposition product. Morozova [12] and Niinistö [8,

15] reported that bis(Cp)HfMe$_2$ pyrolysis began in the 350 – 450 °C temperature range.

Morozova used a mass spectrometer attached to the reaction chamber to analyze gas

phase species during the decomposition and observed HCp as a volatile product around 350 °C and then CH_4 around 450 °C.

Experimental details

Precursor synthesis

All precursors were synthesized under nitrogen atmosphere in a dry box. Purities of the synthesized compounds were determined by ^{1}H NMR analysis. Bis(MeCp)HfMe$_2$ was synthesized according to the method of Niinisto and colleagues [4]. The product was an oily orange solid. Bis(Cp)HfMe$_2$ was synthesized according to the method of Samuel and Rausch [16]. The reaction product was a crystalline white solid. Bis(Cp)Hf^{n}Bu$_2$ was synthesized according to the method of Burlakov and colleagues [5], and the product was an orange solid.

Characterization

Thermal stability of the compounds was evaluated by thermogravimetric analysis (TGA 1000, Instrument Specialists, Twin Lakes, WI, USA). Approximately 25 mg of the compound was loaded into an aluminum sample pan for analysis. Samples were heated to 600 °C at a rate of 20 °C/min in a flow of 10 sccm N_2.

Elemental identification and chemical bonding states were determined through X-ray photoelectron spectroscopy (Ulvac-PHI Versaprobe XPS Microprobe, Chanhassen, MN, USA). A 25 W monochromatic Al K$_\alpha$ x-ray source was used. The x-ray beam diameter was 100 μm. Photoelectrons emitted from the sample at 45° takeoff angle were

collected into a spherical capacitor analyzer operating in constant pass energy mode. The

pass energies of survey and high-resolution scans were 187.50 eV and 23.50 eV,

respectively. Surface charge compensation was achieved with a neutralization system

comprised of low energy electrons and Ar^+ ions.

Liquid phase casting and annealing

Silicon (100) substrates were used for all samples. Several substrates were dipped

in a 2 vol% HF/DI water solution to etch off the native oxide (referred to as H-Si

substrate). The etched sample was then loaded into inert environment within a few

minutes to prevent re-oxidation.

All samples were prepared in a dry box under nitrogen ambient. $Bis(Cp)HfMe_2$

was dissolved in anhydrous toluene, which produced a clear solution. Approximately

four drops of solution were pipetted onto 1 cm^2 substrates. The sample was placed on a

hot plate and heated on the LOW heat setting. The sample was removed from the heat

when there was no more visible liquid on the surface. The as-formed films were dull

gray in color. $Bis(MeCp)HfMe_2$ was dissolved in tetrahydrofuran and pipetted onto

substrates as mentioned above. The samples were heated on a hot plate until there was

no more visible liquid on the surface. Additional solution was dropped on the sample

while it was being heated. Bubbles were observed on the surface. There were orange

colored particles on the surface. Samples were then allowed to cool for several minutes

before removal from the dry box. After removal from the hot plate, samples cooled for 5

minutes and were transferred to the annealing chamber or XPS system within several

minutes.

Samples were annealed in a high-vacuum chamber with base pressure of approximately 10^{-7} Torr. The samples were heated by a ceramic heater located approximately 1 cm away from the sample. Bis(Cp)HfMe$_2$ was annealed for 20 minutes at 600 °C, and bis(MeCp)HfMe$_2$ was annealed for 20 minutes at 500 °C. After annealing, the samples cooled in the loading chamber and were then transferred to the XPS system within five minutes.

Results and discussion

Thermal stability

Bis(Cp)Hf^{n}Bu$_2$ melted during handling while preparing a sample for thermogravimetric analysis (TGA). Upon solidification orange particles were observed, and we assumed the sample decomposed.

Figure 6.2 contains thermogravimetric analysis data for a sample of bis(MeCp)HfMe$_2$. Sample weight began to decrease at approximately 50 °C. The weight continued to decrease until the end of the scan, and approximately 60% of the mass of the sample remained at the end of the run. An inflection point was observed at approximately 225 °C, and was attributed to decomposition of the sample and loss of constituent species. Weight loss at temperatures less than 225 °C was attributed to evaporation of the compound.
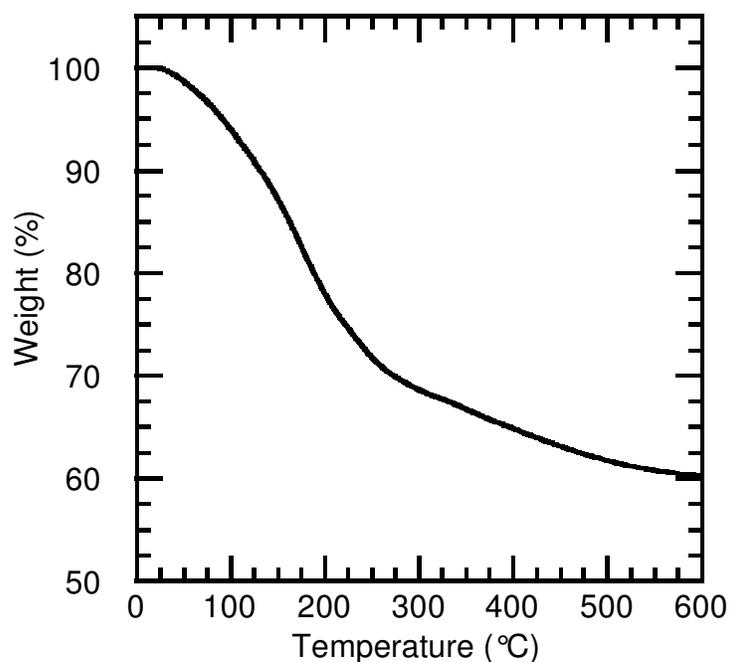
Figure 6.2 - TGA curve for bis(MeCp)HfMe$_2$ shows onset of material decomposition at approximately 225 °C. Sample was prepared in air.

The data in Figure 6.2 was not consistent with previous reports of TGA analysis of bis(MeCp)HfMe$_2$. Data presented by Niinisto [4] and Rushworth [13] showed that weight loss was not observed until the sample was heated to approximately 125 °C. In addition the data suggested that the samples fully evaporated without decomposition.

Our observations were correlated to changes in the compound due to ambient exposure. During preparation of the TGA sample, a spatula was used to transfer the compound to the sample pan. The portions of the sample which made contact with the spatula changed from transparent orange to opaque white. The orange and white regions were analyzed by XPS to identify differences in their chemical compositions. Figure 6.3 contains XPS survey spectra collected from each region. Peaks observed in each spectrum were assigned to hafnium, oxygen, and carbon, and suggested that no

contaminants were introduced to the sample through contact with the spatula. The
intensity of the carbon peak was larger in the spectrum collected from the orange region
than the intensity collected from the white region. Conversely, the intensity of the
oxygen peak was larger in the spectrum collected from the white region than the intensity
collected from the orange region.
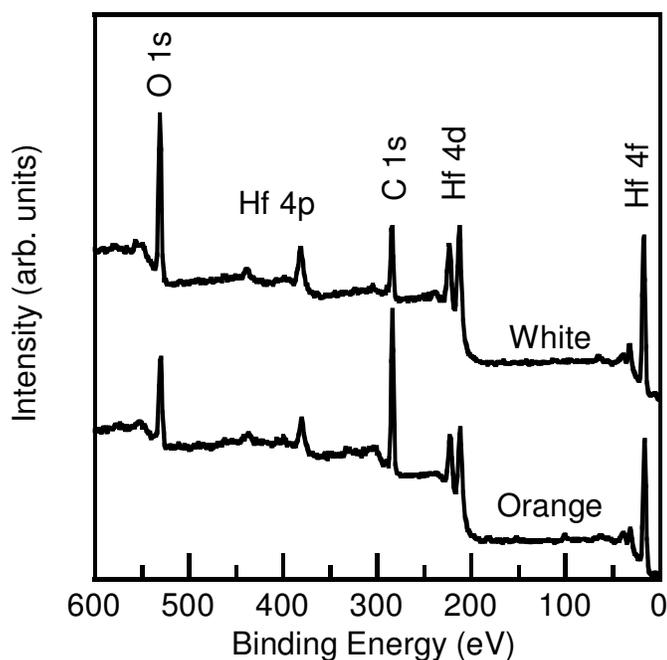
Figure 6.3 - XPS survey spectra of bis(MeCp)HfMe$_2$. Spectrum denoted as "orange" did
not contact tool during preparation of TGA sample. Spectrum denoted as "white" was
collected from portion of sample that rapidly changed color upon contact with spatula.

Annealing of dropcast films

As-received films produced by drop casting were viewed by optical microscope
and appeared discontinuous. Figure 6.4 contains an XPS survey spectrum collected from
a film deposited on H-Si. Peaks were observed that corresponded to Hf, O, C, Si, Cl, Br,

109

and N. The only peaks observed at binding energies higher than 600 eV were attributed

to oxygen and carbon. Chlorine was assumed to originate from the starting reagents in

the synthesis of the compound. The origin of bromine was unknown. Observation of

silicon was attributed to film discontinuity in the analysis area or to analysis of films thin

enough such that photoelectrons generated from the substrate were not completely

attenuated by passing through the film to the spectrometer.
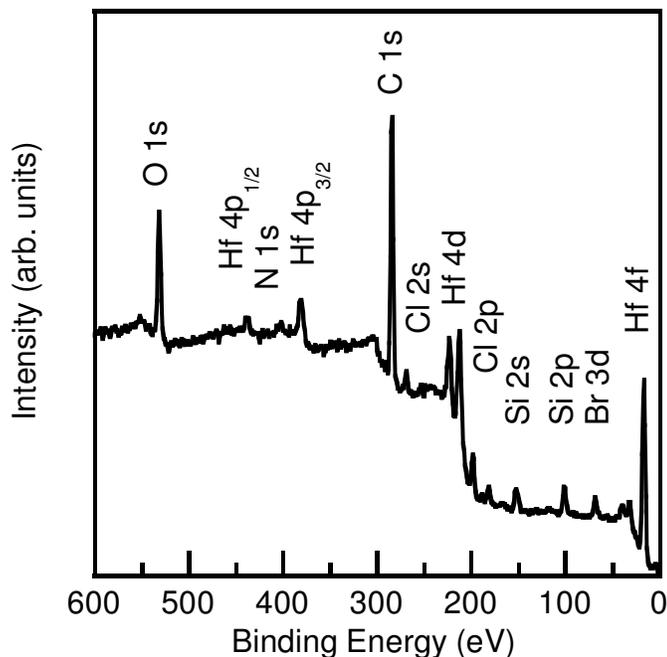
Figure 6.4 - XPS survey spectrum of bis(Cp)HfMe$_2$, dropcast from toluene solution on silicon wafer. Solvent was removed by evaporation.

High-resolution XPS analysis of the Hf 4f, O 1s, and C 1s regions was performed

to understand chemical bonding environments in the drop cast films. Figure 6.5 contains

high-resolution XPS spectra collected from the Hf 4f region of the sample described in

Figure 6.4 (labeled as Sample HfC-5a in Figure 6.5). The Hf 4f region consisted of one

110

set of broad doublet peaks. For comparison, a sputter-deposited hafnium metal film was

analyzed. The native oxide layer was removed by Ar^+ ion beam sputtering in the XPS

analysis chamber. The metal film was then exposed to air for approximately 20 minutes

and then re-analyzed. After sitting in air, the spectrum of the Hf 4f region had two sets of

peaks, suggesting formation of an oxide layer. The spectrum from sample HfC-5a

exhibited peaks at binding energies between the peaks related to the metallic and oxide

bonding states, suggesting that even after our sample was out in air, it was not fully

oxidized.
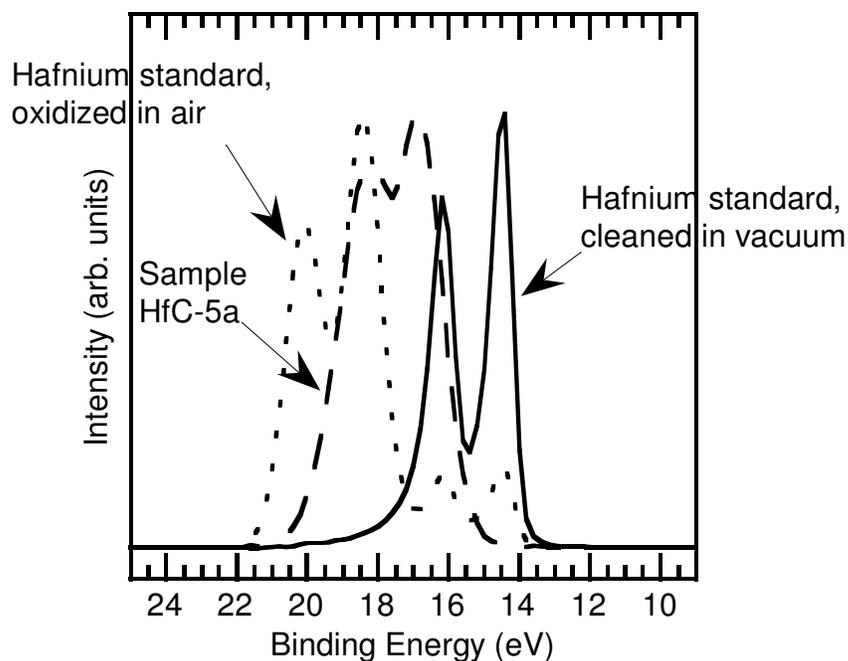
Figure 6.5 – XPS spectra of Hf 4f region from bis(Cp)HfMe$_2$ (labled as Sample HfC-5a).
Spectra from metallic hafnium film and oxidized hafnium metal film included for
comparison.

Figure 6.6 contains the XPS spectra in the C 1s and O 1s regions of the same sample referenced in Figure 6.5. The C 1s region consisted of one large peak at 284.46 eV. Initially, we thought there would be a peak near 280 eV, similar to reported values for metal carbides. However, reported C 1s binding energies for ferrocene and other first row metallocenes are in the range 284.6-285.1 ±0.3 eV [17]. The O 1s spectrum can be deconvoluted into two peaks. The shoulder at low binding energy corresponds to a metal oxide bond. The data from Figures 6.5 and 6.6 suggest that the hafnium is partially oxidized but may still retain the cyclopentadienyl ring.
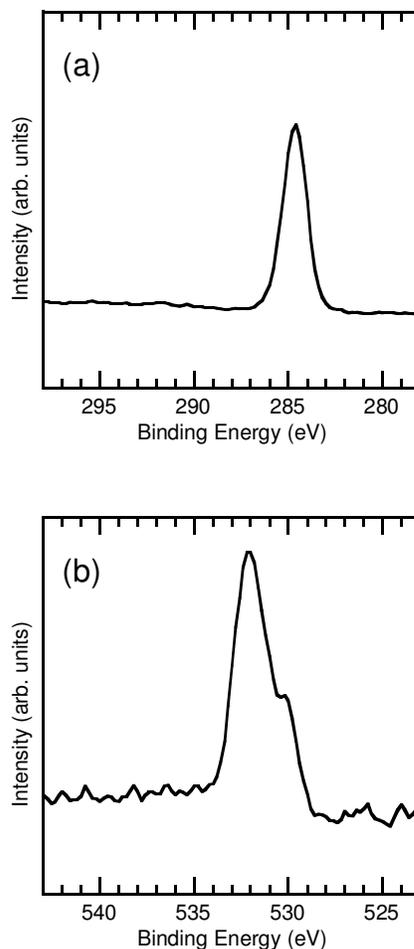
Figure 6.6 – High resolution XPS spectra collected from (a) C 1s and (b) O 1s regions in bis(Cp)HfMe$_2$, referenced in Figures 6.4 and 6.5. Sample was dropcast from toluene solution on silicon wafer. Solvent was removed by evaporation.

Conclusions

Three hafnocene compounds were evaluated for use as CVD precursors to HfC or HfOC films. Bis(Cp)Hf^{n}Bu$_2$ and bis(MeCp)HfMe$_2$ are superior to bis(Cp)HfMe$_2$ in that they melt near room temperature. They would be well-suited for a bubbler type delivery system. One concern with bis(Cp)Hf^{n}Bu$_2$ is its thermal stability. Similar compounds are prone to β-hydride elimination, and it is reasonable to assume that process control would be difficult if the precursor decomposed unexpectedly.

Previous reports suggest that bis(MeCp)Me$_2$ and bis(Cp)HfMe$_2$ thermally decompose at nearly the same temperature. There is a definite advantage in using the methylated Cp compound due to its lower melting temperature, but there is a cost tradeoff. The reaction to add the methyl group to the Cp group has a low yield, so more raw material is required to achieve an adequate supply for use in a bubbler. Since hafnium is typically expensive, the bis(MeCp)Me$_2$ compound may not be cost-effective.

REFERENCES

1.   Bargeron, C.B., R.C. Benson, A.N. Jette, and T.E. Phillips, *Oxidation of Hafnium Carbide in the Temperature-Range 1400-Degrees to 2060-Degrees-C.* Journal of the American Ceramic Society, 1993. **76**(4): p. 1040-1046.

2.   Pierson, H.O., *Handbook of Refractory Carbides and Nitrides.* Materials Science and Process Technology Series. 1996, Westwood, NJ: Noyes Publications.

3.   Sigma-Aldrich. *557056 Dimethylbiscyclopentadienyl hafnium IV.* 2008 [cited 2008 June 9]; Available from: http://www.sigmaaldrich.com/catalog/search/ProductDetail/ALDRICH/557056.

4.   Niinisto, J., M. Putkonen, L. Niinisto, F.Q. Song, P. Williams, P.N. Heys, and R. Odedra, *Atomic layer deposition of HfO2 thin films exploiting novel cyclopentadienyl precursors at high temperatures.* Chemistry of Materials, 2007. **19**(13): p. 3319-3324.

5.   Burlakov, V.V., T. Beweries, V.S. Bogdanov, P. Arndt, W. Baumann, P.V. Petrovskii, A. Spannenberg, K.A. Lyssenko, V.B. Shur, and U. Rosenthal, *Synthesis and Isolation of Di-n-butylhafnocene and Its Application as a Versatile Starting Material for the Synthesis of New Hafnacycles.* Organometallics, 2009. **28**(9): p. 2864-2870.

6.   Strem Chemicals, Inc. *Catalog.* 2009 [cited 2009 November 24]; Available from: http://www.strem.com/catalog/v/72-0700/26/.

7.   SAFC. *SAFC Hitech - Hafnium Products - Bis(methyl-η5-cyclopentadienyl)dimethylhafnium.* 2009 [cited 2009 November 24]; Available from: http://www.sigmaaldrich.com/safc-hitech/en-us/home/overview/products/hafnium/bis-methyl-n5-cyclopentadienyl.html.

8.   Niinisto, J., M. Putkonen, L. Niinisto, S.L. Stoll, K. Kukli, T. Sajavaara, M. Ritala, and M. Leskela, *Controlled growth of HfO2 thin films by atomic layer deposition from cyclopentadienyl-type precursor and water.* Journal of Materials Chemistry, 2005. **15**(23): p. 2271-2275.

9.   Dezelah, C.L., J. Niinisto, K. Kukli, F. Munnik, J. Lu, M. Ritala, M. Leskela, and L. Niinisto, *The Atomic Layer Deposition of HfO2 and ZrO2 using Advanced Metallocene Precursors and H2O as the Oxygen Source.* Chemical Vapor Deposition, 2008. **14**(11-12): p. 358-365.

10.   Chang, B.H., H.S. Tung, and C.H. Brubaker, *The Thermal-Decomposition of Dibutylbis(Eta-5-Cyclopentadienyl)Titanium, Other Dialkyl Metallocenes, and Di(Eta-5-Pentamethylcyclopentadienyl)Titanium.* Inorganica Chimica Acta-Articles, 1981. **51**(2): p. 143-148.

11.   Mcdermott, J.X., M.E. Wilson, and G.M. Whitesides, *Synthesis and Reactions of Bis(Cyclopentadienyl)Titanium(Iv) Metallocycles.* Journal of the American Chemical Society, 1976. **98**(21): p. 6529-6536.

12.   Morozova, N.B., K.V. Zherikova, I.A. Baidina, S.V. Sysoev, P.P. Semyannikov, L.V. Yakovkina, T.P. Smirnova, N.V. Gelfond, I.K. Igumenov, G. Carta, and G. Rossetto, *Volatile hafnium(IV) compounds with beta-diketonate and cyclopentadienyl derivatives.* Journal of Physics and Chemistry of Solids, 2008. **69**(2-3): p. 673-679.

13.   Rushworth, S., K. Coward, H. Davies, P. Heys, T. Leese, L. Kempster, R. Odedra, and P. Williams, *Thermal stability studies for advanced Hafnium and Zirconium ALD precursors.* Surface & Coatings Technology, 2007. **201**(22-23): p. 9060-9065.

14.   Lang, H. and D. Seyferth, *Pyrolysis of Metallocene Complexes (Eta-C5H4R)2Mr2' - an Organometallic Route to Metal Carbide (Mc) Materials (M = Ti, Zr, Hf).* Applied Organometallic Chemistry, 1990. **4**(6): p. 599-606.

15.   Niinisto, J., M. Putkonen, L. Niinisto, K. Arstila, T. Sajavaara, J. Lu, K. Kukli, M. Ritala, and M. Leskela, *HfO2 films grown by ALD using cyclopentadienyl-type precursors and H2O or O-3 as oxygen source.* Journal of the Electrochemical Society, 2006. **153**(3): p. F39-F45.

16.   Samuel, E. and M.D. Rausch, *Pi-Cyclopentadienyl and Pi-Indenyl Compounds of Titanium, Zirconium, and Hafnium Containing Sigma-Bonded Organic Substituents.* Journal of the American Chemical Society, 1973. **95**(19): p. 6263-6267.

17.	Barber, M., J.A. Connor, L.M.R. Derrick, M.B. Hall, and I.H. Hillier, *High-Energy Photoelectron Spectroscopy of Transition-Metal Complexes .2. Metallocenes.* Journal of the Chemical Society-Faraday Transactions Ii, 1973(4): p. 559-562.

CHAPTER VII

CONCLUSIONS AND FUTURE WORK

Introduction

Ceramics comprise a large subset of materials that may be exploited for thermal protection and electrical insulation. Traditional processing of ceramics involves high temperature powder pressing, and alternative technologies are desirable for fabrication of complex structures and reduction in energy costs. In this work, materials in the Al-C-O and Hf-C-O systems were investigated. Mixed-ligand precursors were developed for production of AlO_xC_y and HfO_xC_y films by vapor and liquid phase deposition methods.

Summary of this work

MOCVD aluminum oxycarbide films produced from dimethylaluminum isopropoxide

Aluminum oxycarbide (AlO_xC_y) films were fabricated in a high-vacuum chemical vapor deposition reactor (CVD) via thermal decomposition of dimethylaluminum isopropoxide (DMAI) precursor. This precursor was chosen because it has similar properties to both trimethylaluminum (TMA) and aluminum tri-isopropoxide (ATI). DMAI is attractive because it contains oxygen within the precursor, is more stable than TMA, and also exhibits a higher vapor pressure than ATI.

Films were deposited under conditions described in Chapter II. The deposition rate suggested that film deposition was limited by surface reactions. Film thickness

uniformity was correlated to variations in the substrate temperature. Elemental analysis confirmed that films were composed of aluminum, oxygen, and carbon as expected. Optical models of the deposited films were also developed.

Film carbon content increased as deposition temperature was increased, but overall stoichiometries were unexpected according to the stoichiometry of the precursor. Analysis of fluxes within the reactor suggested that trace oxygen-containing gas species present in the reactor at its base pressure were participating in the deposition process. These trace gases contributed oxygen atoms to the growing film such that the oxygen/aluminum ratio in the film was greater than the ratio in the precursor molecule. Chemical bonding within the deposited films changed with deposition temperature. Bonding between aluminum and carbon atoms was observed for only deposition temperatures of 538 °C and higher. This observation suggested incomplete decomposition of methyl groups attached to the aluminum atom.

Films were evaluated on their performance as dielectric materials in metal-oxide-semiconductor capacitors. The dielectric constant of each film was comparable to that of silicon dioxide, suggesting that the films in this study were not suitable as replacements to silica in microelectronics devices. In addition, the slow deposition rate of the oxycarbide films is likely not suitable for thermal applications in which large areas require uniform coatings up to several hundred micrometers thick.

Dropcast hafnium oxycarbide films produced from metallocene precursors

We sought a liquid phase CVD precursor for deposition of hafnium carbide (HfC) or oxycarbide (HfO_xC_y) films. The ideal precursor would contain only hafnium, oxygen,

carbon, and hydrogen so that it could be used in a thermal decomposition process similar to that of the aluminum oxycarbide films. Hafnium metallocenes were investigated due to their thermal stability and the opportunity for modification.

Dimethyl hafnocene (bis(Cp)HfMe$_2$) was chosen as a base compound, where Cp=C$_5$H$_5$ and Me=CH$_3$. Two derivatives were also synthesized. Alkyl groups were either attached to the Cp group or the hafnium atom to lower the melting point of the base compound. Compounds were not produced in sufficient quantities for use in a CVD bubbler system due to material cost and synthesis yield.

Each of the compounds readily oxidized in air, so all sample preparations were performed under inert environment. Bis(Cp)Hf^{n}Bu$_2$ was removed from consideration due to its instability during routine handling, where Bu=C$_4$H$_9$. Films were produced from bis(MeCp)HfMe$_2$ and bis(Cp)HfMe$_2$ by dissolving the precursors in solvents and dropping the solution on silicon substrates. The films were discontinuous and oxidized while sitting in air. Chemical state analysis suggested that the methyl groups attached to the hafnium atom preferentially oxidized while the Cp group remained intact.

Future work

Based on the experience and information gained from this work, we make the following suggestions for future investigations into these materials and processes:

(1) Synthesis and investigation of monomethylaluminum di-isopropoxide (MADI) for the production of AlO$_z$C$_y$ films. MADI is a combination of the dimethylaluminum isopropoxide (DMAI) precursor used in this work and aluminum tri-isopropoxide (ATI). MADI possesses an O/Al ratio of 2, which suggests that it may be used for deposition of

stoichiometric carbon-free Al_2O_3 films via thermal decomposition. The vapor pressure of MADI is expected to be higher than that of ATI.

(2) Explore the parameter space to optimize deposition rate of films from DMAI. In the current work, deposition rates were in the range of ~ 1 Å/min based on the chosen process conditions. This is a very slow process and likely not cost-effective for most applications. Characterization of thin films also presented difficulties because of the resolution of many measurement techniques. Several possibilities for increasing deposition rate are: increase of precursor transport to the reactor through adjustment of bubbler temperature or carrier gas flow rate, introduction of a co-reactant gas that provides a lower kinetic barrier for film deposition, or higher deposition temperatures.

(3) Pursue alternative processing techniques and materials for microelectronics applications. Although aluminum oxide was one of several candidates to replace silicon dioxide in transistor devices, the microelectronics industry has recently adopted hafnium oxide-based dielectrics. Hafnia is superior to alumina in that hafnia exhibits a higher dielectric constant and therefore a longer lifetime for process scaling. Dielectrics are also typically deposited by atomic layer deposition (ALD), which allows more control over film thickness than traditional CVD. ALD processing using DMAI in conjunction with hafnium-based precursors may be interesting because alumina films tend to be amorphous while hafnia films are crystalline. Film crystallinity provides pathways for undesirable electron transport through the dielectric.

(4) Construction of a differential pumping system attached to the quadrupole mass spectrometer for the analysis of evolved gases during chemical vapor deposition runs. Identification of byproduct species can provide insight into reactions and their

mechanisms occurring in the reactor. The pressure in the reaction chamber during a deposition exceeds the limit for operation of the mass spectrometer in its current setup. An aperture and differential pumping station would allow the spectrometer to operate at reduced pressure while sampling gases present in the chamber.

(5) Investigate zirconium-based precursors as model systems prior to synthesis of hafnium-based precursors. Hafnium compounds tend to cost more than their zirconium analogs due to the relative rarity of hafnium compared to zirconium. Zirconium and hafnium are similar chemically and often can be synthesized using similar methods.